Research Square

Preprints are preliminary reports that have not undergone peer review.
They should not be considered conclusive, used to inform clinical practice,
or referenced by the media as validated information.

Resolved coastal dynamics reduce the Peru coastal warm SST bias in an eddy-resolving ICON simulation

Dakuan Yu

dakuan.yu@mpimet.mpg.de

Max Planck Institute for Meteorology https://orcid.org/0000-0002-3133-1414

Wolfgang Müller

Max Planck Institute for Meteorology

Article

Keywords:

Posted Date: August 26th, 2026

DOI: https://doi.org/10.21203/rs.3.rs-10803782/v1

License: This work is licensed under a Creative Commons Attribution 4.0 International License.
Read Full License

Additional Declarations: There is **NO** Competing Interest.

Resolved coastal dynamics reduce the Peru coastal warm SST bias in an eddy-resolving ICON simulation

Dakuan Yu[1] and Wolfgang A. Müller[1]

[1]Max Planck Institute for Meteorology, Hamburg, Germany.

Corresponding author: Dakuan Yu (dakuan.yu@mpimet.mpg.de)

Abstract

Warm sea-surface temperature (SST) biases persist in coupled climate models of the eastern tropical Pacific, particularly along the narrow Peru coastal upwelling system. We investigate why an eddy-resolving ICON simulation, with nominal atmospheric and oceanic grid spacings of 10 and 5 km, respectively, reduces this bias relative to a coarser 160 km / 40 km ICON configuration and the CMIP6 multimodel mean. Observational, reanalysis, and satellite products are used to diagnose fixed 0–50 m temperature tendencies within the Peru coastal band. The eddy-resolving configuration removes the strong nearshore warm bias but leaves a modest cold bias. Sharper Andes and coastal geometry support stronger upwelling-favorable wind stress and offshore Ekman transport, strengthening nearshore upwelling, coastal currents, and SST cooling. Mean advection and lower-boundary exchange provide the primary coherent cooling, especially through cross-shore transport and vertical exchange. Differences in surface-flux tendency and transient heat-flux convergence between the ICON configurations are comparatively small. An independent HighResMIP2 simulation shows a similar dynamical pathway. Resolving the coupled coastal topography–wind–upwelling–current–advection system in high-resolution modeling is therefore central to reducing eastern Pacific coastal SST biases, although cooling in the eddy-resolving ICON simulation exceeds the reference estimate.

1 Introduction

The Peru coastal upwelling system is a major eastern-boundary current region with disproportionate climatic, biogeochemical, and socio-economic importance. Persistent equatorward winds along the west coast of South America drive offshore Ekman transport and nearshore upwelling, maintaining cold sea-surface temperatures (SSTs), a sharp coastal SST front, and a nutrient supply that supports one of the world's most productive marine ecosystems and major global fisheries[1–3]. The cold coastal ocean also anchors a persistent marine stratocumulus deck, whose shortwave reflection strongly shapes the regional surface energy balance and lower-tropospheric stability[4–6]. Although the upwelling zone is geographically narrow, its influence extends beyond the coastal ocean through its effects on tropical Pacific SST gradients, marine cloud radiative properties, tropical rainfall, and the regional structure of the intertropical convergence zone.

Despite this importance, coupled climate models have long struggled to simulate the Peru and eastern tropical Pacific climate state. A persistent warm SST bias is common along the Peru coast and across the eastern tropical Pacific in climate models, contributing to errors in the equatorial cold tongue, marine cloud cover, tropical rainfall, and the double-ITCZ bias[6–10]. The persistence of this warm bias across model generations suggests that the problem is not controlled by a single process, but by the coupled representation of coastal winds, ocean upwelling, horizontal advection, clouds, and surface heat fluxes.

Several processes may contribute to this bias. Insufficient stratocumulus cloud cover increases shortwave radiation into the ocean, while boundary-layer errors modify cloud radiative effects and turbulent heat fluxes[4,5,11,12]. Weak or displaced coastal winds reduce offshore Ekman forcing and upwelling, particularly when coarse atmospheric grids smooth the Andes and distort the land–sea contrast[10,13,14]. Ocean circulation errors weaken nearshore upwelling, coastal currents, and the horizontal advection of cold water. Mesoscale and transient processes further redistribute heat between the nearshore upwelling zone and the offshore stratocumulus region[15–18].

High-grid-resolution coupled models provide a more direct means of testing these pathways. Finer atmospheric grids sharpen the representation of the Andes, coastline, coastal pressure gradients, and nearshore wind stress, while finer ocean grids resolve sharper coastal fronts, more realistic nearshore currents, and a more active mesoscale circulation[10,13,14,19]. However, interactions among these processes make it difficult to determine which cooling pathway dominates the reduction of the warm SST bias in high-grid-resolution coupled models. Here we use an eddy-resolving ICON simulation, with nominal grid spacings of approximately 10 km in the atmosphere and 5 km in the ocean, to examine why the strong Peru coastal warm SST bias is substantially reduced relative to a coarser ICON configuration and the CMIP6 multimodel mean. We first place this reduction in a broader model context by showing that the Peru coastal warm bias decreases progressively from CMIP6 to HighResMIP1 and HighResMIP2. We then diagnose a consistent 0–200 km Peru coastal band and compare the two ICON configurations with observational or reanalysis products for SST, precipitation, topography, winds, upwelling, currents, 0–50 m-averaged temperature tendencies, surface fluxes, and cloud-radiative properties. The analysis is organized around three questions: how model configuration and grid resolution change the coastal topography–wind–upwelling pathway; whether the SST-bias reduction is maintained by mean advection and upwelling, transient heat-flux convergence, or surface fluxes; and how clouds and shortwave cloud radiative effects modulate the coastal heat balance.

2 Results

2.1 Reduction of the Peru coastal SST warm bias

Figure 1 places the SST biases of the two ICON configurations in the broader context of CMIP6, HighResMIP1, HighResMIP2, and MPI-ESM1-2-XR. The observed SST climatology shows the eastern Pacific cold tongue and the Peru coastal upwelling signature, with a narrow band of cool water adjacent to the South American coast and warmer water offshore. The bias panels report two spatial means: the coastal bias within the 0–200 km Peru coastal band and the domain bias over the full plotted map domain.

The multimodel means show a progressive transition from warm to cold SST biases as model resolution increases. The coastal bias decreases from approximately +2.67 °C in CMIP6 to +1.73 °C in HighResMIP1 and −1.12 °C in HighResMIP2. The corresponding domain bias decreases from approximately +1.54 °C to +1.01 °C and −0.60 °C, respectively. The larger bias magnitudes within the coastal band show that the resolution-dependent change is strongest in the narrow Peru upwelling region. These values indicate that the long-standing coastal warm bias is progressively reduced from CMIP6 to HighResMIP1 and HighResMIP2, with the HighResMIP2 mean shifting to a cold bias both near the coast and across the plotted domain.

The individual-model comparison shows the same progression. The coarser ICON configuration has a coastal bias of approximately +2.39 °C and a domain bias of approximately +2.05 °C. MPI-ESM1-2-XR reduces these warm biases to approximately +1.30 °C in the coastal band and +0.57 °C over the domain. The eddy-resolving ICON simulation shifts to a cold bias of approximately −0.67 °C in the coastal band and −0.40 °C over the domain. The transition between the two ICON configurations therefore represents the clearest individual shift in this comparison from a warm-biased coarser coastal state to a cold-biased eddy-resolving state.

Importantly, the reduced Peru coastal SST bias in the eddy-resolving ICON simulation cannot be attributed to a uniformly cooler global ocean. Over 1982–2014, the global-mean SST bias is only −0.05 °C in the eddy-resolving configuration, whereas the coarser configuration has a more negative global-mean bias of −0.20 °C despite retaining a coastal warm bias of +2.39 °C. After removing these global-mean offsets, the coastal biases remain −0.62 °C in the eddy-resolving configuration and +2.59 °C in the coarser configuration. The improvement in the eddy-resolving simulation therefore primarily reflects regional coastal processes rather than a global-mean temperature shift. Supplementary Fig. 1 shows a parallel improvement in precipitation: the eddy-resolving simulation nearly removes the coastal precipitation wet bias while retaining a modest domain-mean wet bias. This reduction is consistent with a broader improvement in the eastern Pacific coupled climate state.

The spatial pattern and the stronger coastal-band response provide an initial indication of the mechanism. The largest bias reduction is concentrated in the narrow Peru coastal upwelling zone rather than distributed uniformly across the broader eastern Pacific. This localization points to a coastal dynamical pathway involving nearshore winds, upwelling, currents, and ocean advection, which is examined in the following sections.

2.2 Sharper topography and stronger coastal wind forcing

The atmospheric side of the coastal dynamical pathway is shown in Fig. 2. The eddy-resolving ICON configuration better resolves the steep Andes and the coastal geometry of western South America than the coarser configuration. The land–sea transition is sharper and the coastal orographic barrier is more realistic. This configuration- and resolution-related contrast is dynamically important because the Andes constrain the low-level flow, shape coastal pressure gradients, and help organize the alongshore winds that drive offshore Ekman transport.

The 10 m wind and nearshore wind-stress patterns show a corresponding configuration dependence. In the coarser ICON configuration, the smoother coastal orography weakens and broadens the

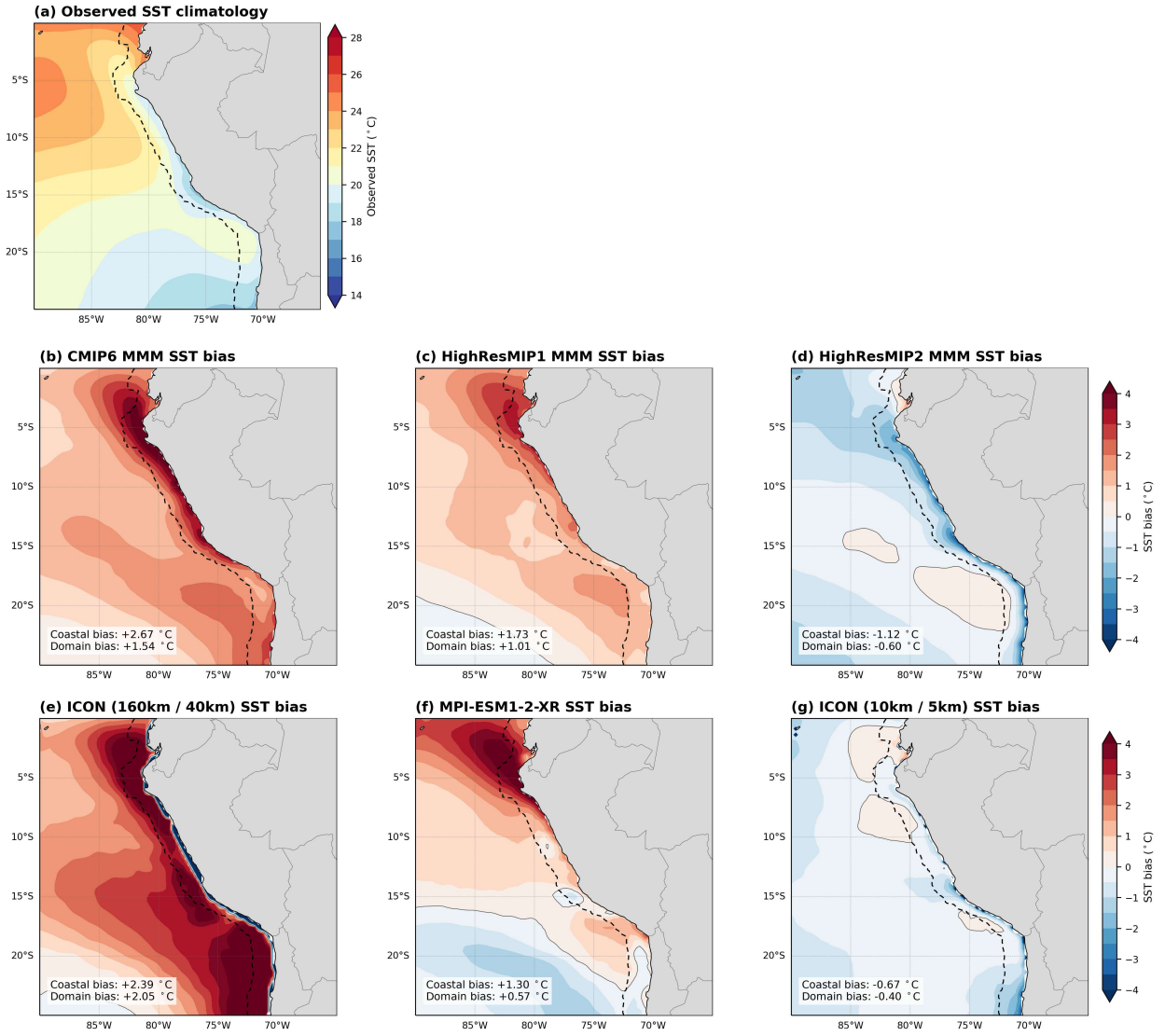

Figure 1: **SST climatology and SST bias in the Peru/eastern Pacific coastal region across CMIP6, HighResMIP, and ICON simulations.** Panel (a) shows observed annual-mean SST from NOAA OISST over 1982–2014. Panels (b)–(g) show annual-mean SST bias relative to OISST for the CMIP6 multimodel mean, HighResMIP1 multimodel mean, HighResMIP2 multimodel mean, ICON (160 km / 40 km), MPI-ESM1-2-XR, and ICON (10 km / 5 km). ICON resolutions are given as atmospheric / oceanic nominal grid spacing. All fields are displayed on the NOAA OISST 0.25° grid. Positive values indicate warm SST bias and negative values indicate cold SST bias. Labels in panels (b)–(g) report the mean SST bias within the 0–200 km Peru coastal band (coastal bias) and over the full plotted map domain (domain bias). The dashed black line marks the offshore edge of the coastal band, which extends from 25°S to the equator.

nearshore wind-stress maximum. This reduces the focused Ekman divergence that sustains coastal upwelling and spreads the wind forcing over a broader offshore region. In the eddy-resolving configuration, by contrast, the nearshore winds are stronger and more coastally confined, producing enhanced equatorward wind stress along the Peru coast. This behavior is consistent with previous studies showing that atmospheric resolution and topographic representation strongly affect eastern-boundary wind forcing and SST biases[10,13,14].

Averaged over the 0–200 km coastal band, the upwelling-favorable meridional wind-stress proxy τ_y is approximately 0.035 N m^{-2} in the eddy-resolving ICON configuration, compared with approximately 0.019 N m^{-2} in the coarser configuration and approximately 0.043 N m^{-2} in ERA5 (Fig. 7). In this region, positive τ_y corresponds to equatorward alongshore stress. In the Southern Hemisphere, equatorward alongshore winds drive offshore Ekman transport in the surface layer, promoting upward motion and entrainment of colder subsurface water near the coast. The similarity between the eddy-resolving configuration and ERA5 in the narrow coastal wind-stress structure indicates that the eddy-resolving ICON atmosphere produces a more realistic coastal forcing regime.

The pressure-level meridional wind sections in Supplementary Fig. 2 show that this configuration dependence extends above the surface. The eddy-resolving ICON simulation produces stronger lower-tropospheric northward/equatorward flow over the 0–200 km Peru coastal band than the coarser configuration, particularly in the lower troposphere, and is closer to ERA5. This supports the interpretation that the sharper Andes and coastal geometry in the eddy-resolving configuration improve the coastal wind system across the lower-tropospheric and surface-stress diagnostics.

The wind response provides the first link in the proposed process chain. The eddy-resolving ICON configuration reduces the coastal SST warm bias in the same region where it produces a sharper topography–wind response. The next question is whether the ocean circulation responds in the expected way, through stronger nearshore upwelling and a more realistic coastal current structure.

2.3 Coastal upwelling and nearshore current response

Figure 3 examines the ocean circulation response and defines the Peru coastal upwelling band used for subsequent process diagnostics. In panel (g) of Fig. 3, the ORAS5 cross-shore profiles show that the strongest upward motion is concentrated close to the coast and decays substantially offshore. This motivates the use of a 0–200 km coastal band between 25°S and the equator. The band captures the core of the coastal upwelling system while limiting the influence of the broader offshore ocean.

The eddy-resolving ICON simulation produces stronger and more coastally confined upward motion near 50 m than the coarser configuration. Coastal-band w_{50} is approximately 0.53 m day^{-1} in the eddy-resolving configuration, compared with approximately 0.12 m day^{-1} in the coarser configuration and approximately 0.41 m day^{-1} in ORAS5. Relative to ORAS5, the eddy-resolving configuration slightly overestimates coastal-band w_{50}, suggesting that the restored upwelling pathway may be somewhat too strong. The enhanced upward motion is collocated with the coastal wind-stress maximum in Fig. 2 and with the cold nearshore SST region shown in Fig. 1. This spatial agreement supports the interpretation that stronger upwelling-favorable winds in the eddy-resolving configuration are linked to a stronger dynamical supply of cold subsurface water into the

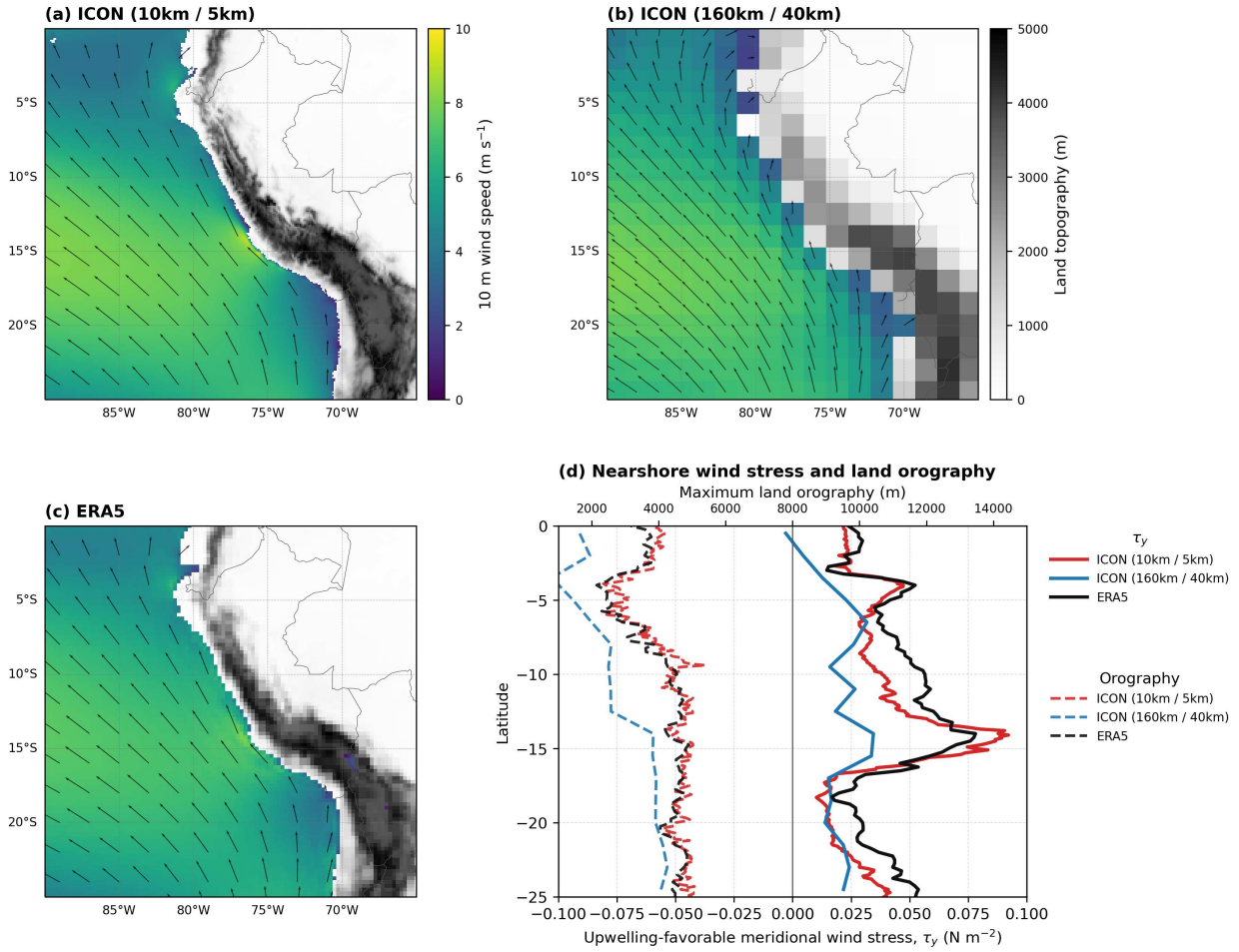

Figure 2: **Topography, 10 m wind, and upwelling-favorable meridional wind-stress proxy.** Panels (a) to (c) compare coastal orography and 10 m winds in ICON (10 km / 5 km), ICON (160 km / 40 km), and ERA5 over 1982–2014. Colors show 10 m wind speed over the ocean and topographic height over land; vectors show 10 m winds. Panel (d) shows latitudinal profiles of coastal orography and nearshore meridional wind stress along Peru. The wind-stress profile is a bulk estimate from 10 m winds, $\tau_y = \rho_{\text{air}} C_d |U_{10}| v_{10}$, using $\rho_{\text{air}} = 1.225$ kg m^{-3} and $C_d = 1.3 \times 10^{-3}$. The profile is averaged over ocean grid cells from the coastline to 200 km offshore between 25°S and 0°; topography is taken from each dataset's own orography field: ICON (10 km / 5 km) uses the ICON external-parameter topography on the native R2B08 atmosphere grid, ICON (160 km / 40 km) uses its native R2B04 atmosphere-grid topography, and ERA5 uses invariant geopotential converted to metres. The orography profile shows the maximum land elevation within 500 km inland from the coastline at each latitude. Positive τ_y denotes northward/equatorward, upwelling-favorable stress along the Peru coast.

upper ocean.

The near-surface horizontal current structure also changes between configurations. The eddy-resolving ICON simulation produces a more coastally organized current structure than the coarser configuration and is closer to ORAS5 in coastal-band current speed. The 0–50 m current speed is approximately 0.037 m s^{-1} in the eddy-resolving configuration, close to approximately 0.038 m s^{-1} in ORAS5, whereas the coarser configuration is approximately 0.054 m s^{-1} in the same band. Thus, the eddy-resolving simulation combines coastally confined upwelling with a more realistic coastal current structure. This matters for SST because the Peru Current and associated nearshore flow influence alongshore cold-water advection, the coastal temperature front, and the background state on which transient heat-flux convergence acts.

The comparison therefore completes the immediate link from wind to ocean: in the eddy-resolving ICON configuration, sharper topography and stronger coastal wind stress are accompanied by stronger nearshore upwelling and a more realistic coastal current structure. The following section tests whether this circulation change produces the mean dynamical cooling required to reduce the coastal SST warm bias.

2.4 Effects of advection and upwelling on cooling

Figure 4 diagnoses the mean advective and upwelling-related temperature tendencies associated with the coastal circulation response. In the eddy-resolving ICON configuration, their sum is strongly negative along the Peru coastal band, indicating coherent cooling by mean advection and lower-boundary exchange. The total tendency is approximately -1.2 °C $month^{-1}$ in the eddy-resolving configuration, compared with approximately -0.15 °C $month^{-1}$ in the coarser configuration and approximately -0.6 °C $month^{-1}$ in ORAS5 (Fig. 7). The strongest cooling in the eddy-resolving simulation is spatially aligned with the enhanced nearshore upwelling and coastally confined current structure shown in Fig. 3, and occurs in the same nearshore region where the SST warm bias is most reduced.

The decomposition shows that cross-shore advection and the vertical lower-boundary exchange tendency provide the main cooling contributions. Cross-shore advection cools the fixed 0–50 m layer when the mean circulation transports colder nearshore or subsurface-influenced water across the coastal temperature gradient. The bulk vertical term cools when upward motion at 50 m replaces water in the fixed-depth layer with colder water from its lower boundary. These two terms are physically linked through the wind-driven coastal upwelling circulation: offshore Ekman transport and coastal divergence require an upward supply of cold water near the coast. Alongshore advection is spatially heterogeneous and partly compensates the cross-shore and vertical cooling where the local temperature gradient and current direction produce warming.

The coarser ICON configuration exhibits weaker and less organized mean dynamical cooling. ORAS5 provides an observationally constrained comparison that supports the presence of a strong coastal dynamical cooling pathway. The spatial coherence of the cooling in the eddy-resolving configuration and its alignment with the wind and upwelling improvements in Figs. 2 and 3 support the interpretation that the bias reduction is tied to a coastally confined mean dynamical cooling pathway. The stronger mean dynamical cooling in the eddy-resolving configuration relative to ORAS5 is

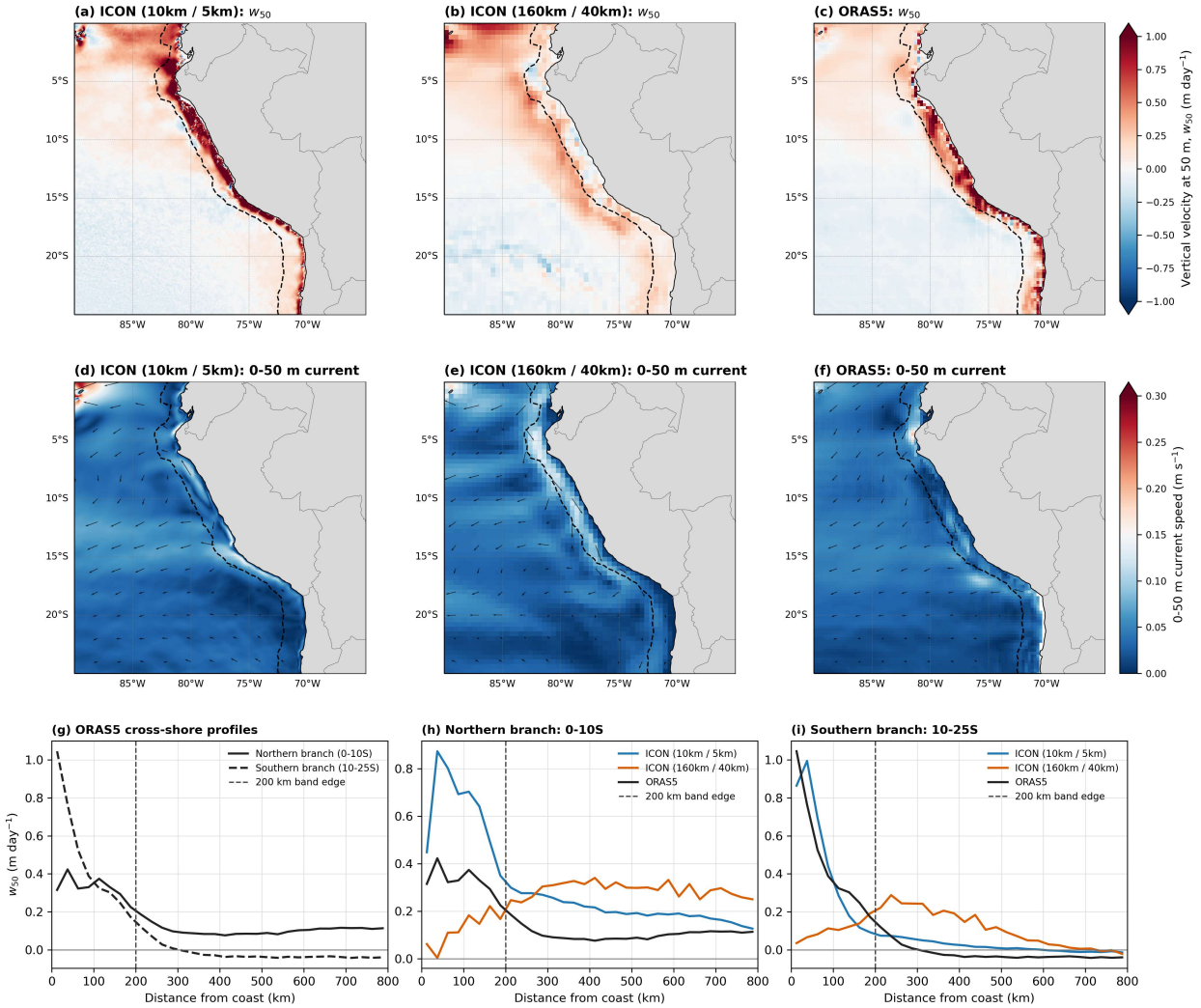

Figure 3: **Coastal upwelling structure and definition of the Peru coastal upwelling band.** Panels (a) to (c) show annual-mean vertical velocity near 50 m, w_{50}, for ICON (10 km / 5 km), ICON (160 km / 40 km), and ORAS5 over 1982–2014. Positive values indicate upward motion. The dashed black line marks the offshore edge of the common Peru coastal upwelling band, defined as 0–200 km from the South American coast between 25°S and the equator. Panels (d) to (f) show annual-mean 0–50 m current speed and current vectors for the same datasets. Panel (g) shows ORAS5 cross-shore w_{50} profiles for the northern branch (0–10°S) and southern branch (10–25°S), which decay substantially within the first approximately 200 km offshore and motivate the fixed-width coastal band. Panels (h) and (i) compare cross-shore w_{50} profiles for ICON (10 km / 5 km), ICON (160 km / 40 km), and ORAS5 in the northern and southern branches. ORAS5 w_{50} is derived from horizontal current divergence integrated from the surface to approximately 50 m.

consistent with the remaining coastal cold bias after the large warm bias in the coarser configuration is removed: the eddy-resolving simulation strongly improves the warm bias but slightly overcools the coastal-band mean because the restored dynamical cooling is stronger than in ORAS5.

2.5 Monthly transient heat redistribution

Figure 5 shows the corresponding monthly transient heat-flux convergence diagnostics. The eddy-resolving ICON configuration contains finer-scale and more spatially structured transient features than the coarser configuration, as expected from its eddy-resolving ocean grid and sharper coastal fronts. These structures indicate that transient variability is physically active in the coastal transition zone and influences local heat redistribution. However, the sign and spatial pattern of the transient tendency differ from the mean dynamical tendency in Fig. 4. Rather than forming a continuous nearshore cooling band, the transient terms are patchy and sign-changing across the alongshore, cross-shore, vertical, and total fields. Local regions of cooling are often adjacent to regions of warming, consistent with transient convergence acting to redistribute heat within and across the coastal transition zone.

The total monthly transient tendency is generally weaker and less spatially coherent than the total mean dynamical cooling in the coastal-band comparison. Figure 7 indicates total monthly transient tendencies of approximately +0.04, +0.17, and +0.12 °C month^{-1} for the eddy-resolving ICON configuration, the coarser ICON configuration, and ORAS5, respectively. The maps also show that the total transient tendency is less spatially organized than the coherent nearshore mean dynamical cooling in Fig. 4. Eddies and transient motions remain dynamically important because they exchange heat between the upwelling zone and offshore waters, modify fronts, alter stratification, and influence air–sea and biogeochemical interactions. In the present monthly diagnostics, their role is best interpreted as heat redistribution and modulation around the upwelling system, while the organized nearshore cooling is supplied by the mean circulation.

A daily versus monthly transient heat-flux sensitivity check for the eddy-resolving ICON configuration is shown in Supplementary Fig. 3. Although local differences appear between the daily-data and monthly-product transient heat-flux tendencies, both estimates retain a relatively weak, patchy structure rather than forming a coherent nearshore cooling band. This supports the interpretation that transient heat-flux convergence acts mainly as a redistribution term in the present diagnostics.

Hence, the eddy-resolving configuration both improves the mean coastal circulation and permits richer transient variability. The SST bias reduction, however, is most directly associated with the restored mean topography–wind–upwelling–current–advection pathway, while monthly transient heat-flux convergence acts mainly as a redistribution and modulation term.

2.6 Surface-flux damping and cloud-radiative effects

Surface fluxes and cloud-radiative effects are shown in Fig. 6, with additional cloud-cover spatial patterns in Supplementary Fig. 4. All surface-flux terms are converted to equivalent temperature tendencies for a fixed 0–50 m upper-ocean layer, with positive values indicating ocean warming.

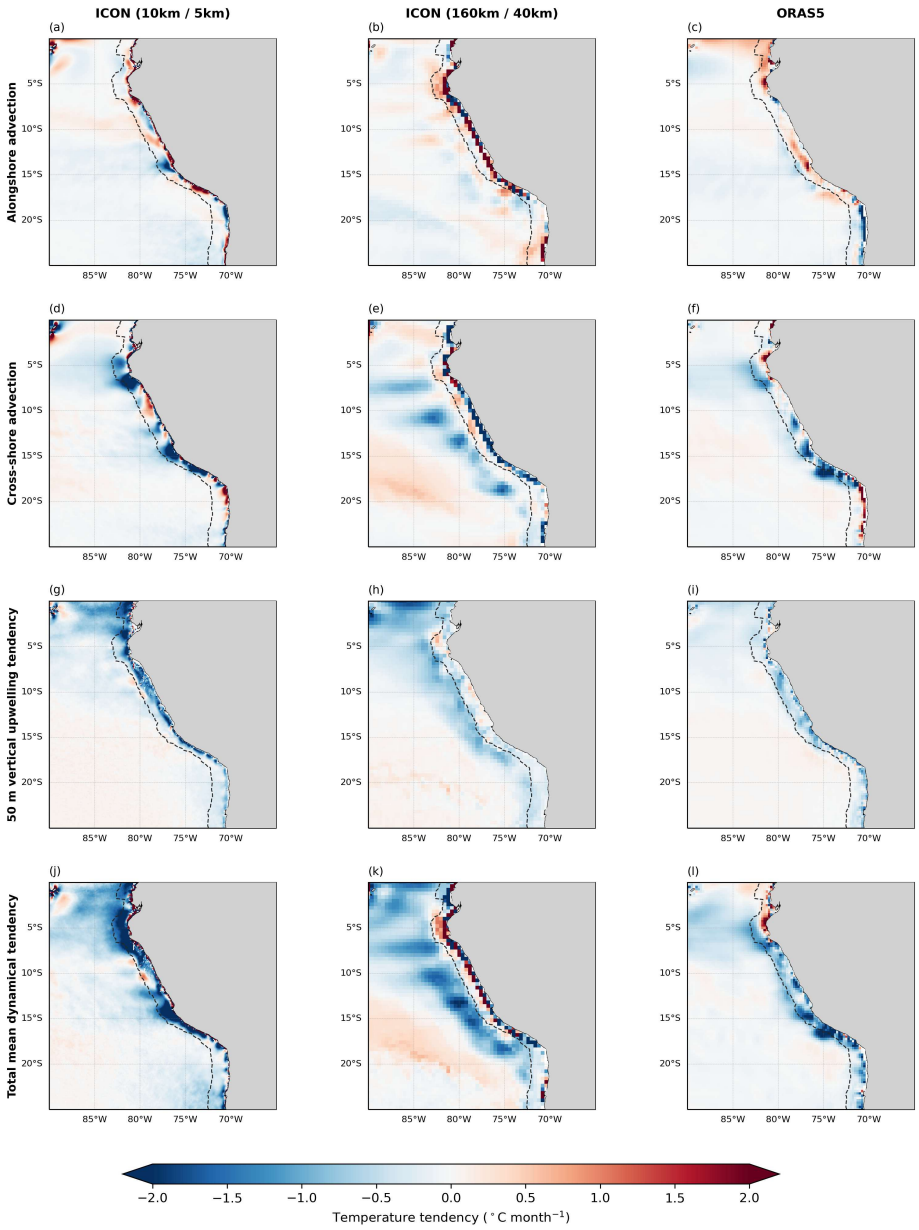

Figure 4: **Mean ocean dynamical temperature tendencies in the Peru coastal upwelling band.** Panels show annual-mean equivalent 0–50 m upper-ocean temperature tendency diagnostics over 1982–2014 for ICON (10 km / 5 km), ICON (160 km / 40 km), and ORAS5. Rows show alongshore mean advection, $-u_{\parallel}\partial T/\partial s$; cross-shore mean advection, $-u_{\perp}\partial T/\partial n$; the 50 m vertical lower-boundary exchange tendency, $w_{50}H^{-1}(T_{50} - T_{0-50})$, with $H = 50$ m; and the total mean dynamical tendency, defined as the sum of the three terms. Negative values indicate cooling and positive values indicate warming. The dashed line marks the 200 km offshore boundary of the Peru coastal upwelling band defined in Fig. 3. Alongshore and cross-shore directions are defined from a smoothed coastline-following coordinate system. ORAS5 w_{50} is diagnosed from horizontal convergence using ORCA025 grid metrics.

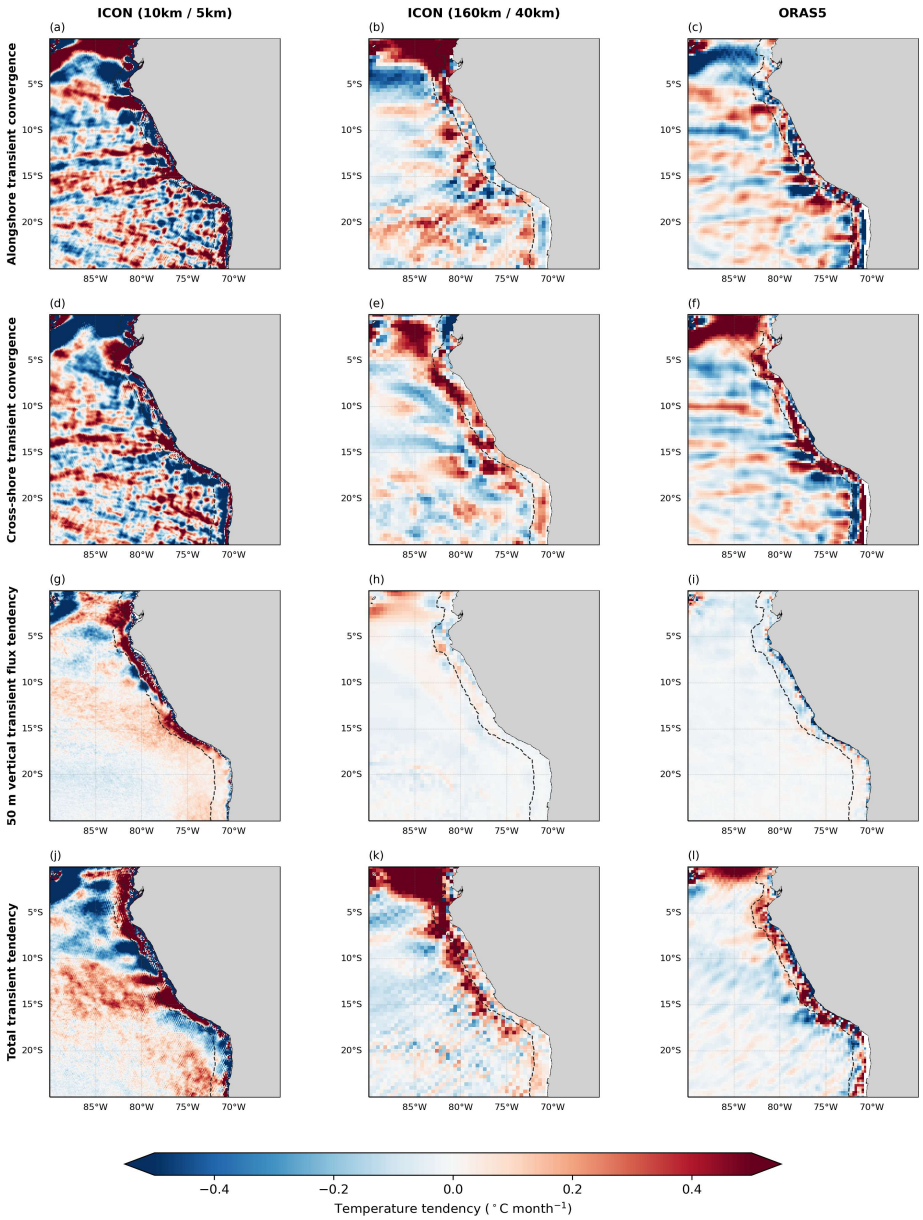

Figure 5: **Monthly transient heat-flux convergence in the Peru coastal upwelling band.** Panels show annual-mean monthly transient temperature tendency diagnostics for a fixed 0–50 m upper-ocean layer over 1982–2014 in ICON (10 km / 5 km), ICON (160 km / 40 km), and ORAS5. Rows show alongshore transient heat-flux convergence, cross-shore transient heat-flux convergence, the 50 m vertical transient flux tendency, and the total monthly transient tendency. The horizontal transient fluxes are based on monthly velocity–temperature covariance terms, $F'_x = \overline{uT} - \overline{u}\,\overline{T}$ and $F'_y = \overline{vT} - \overline{v}\,\overline{T}$. The vertical transient term is $F'_{z,50}/H$, where $F'_{z,50} = \overline{w_{50}T_{50}} - \overline{w}_{50}\,\overline{T}_{50}$ and $H = 50$ m. The total transient tendency is computed from the full horizontal transient heat-flux convergence plus the vertical transient flux tendency. Negative values indicate cooling and positive values indicate warming. The dashed line marks the 200 km offshore boundary of the Peru coastal upwelling band defined in Fig. 3. Alongshore and cross-shore directions use the same smoothed coastline-following coordinate system as Fig. 4.

Over the Peru coastal band, the net surface-flux tendency is positive in both ICON configurations. Surface exchange therefore acts as a warming tendency on the fixed 0–50 m layer and damps the dynamically cooled coastal ocean, while mean ocean dynamics provide the leading cooling source.

In the 0–200 km coastal band, the net surface-flux tendency is approximately +1.0 °C month^{-1} in the eddy-resolving ICON configuration and +0.8 °C month^{-1} in the coarser configuration. The corresponding ERA5 tendency is approximately +1.5 °C month^{-1}. Thus, the difference in net surface warming between the two ICON configurations is small, about 0.2 °C month^{-1}, compared with the much larger difference in total mean ocean dynamical tendency, which changes from weak cooling of approximately −0.15 °C month^{-1} in the coarser configuration to approximately −1.2 °C month^{-1} in the eddy-resolving configuration. The reduction of the coastal SST warm bias between the two configurations is therefore more directly aligned with the restored mean dynamical cooling than with changes in net surface heat flux. Net shortwave radiation warms the layer by approximately +2.6 °C month^{-1} in the eddy-resolving configuration, while latent heat flux cools it by approximately −0.8 °C month^{-1}. The shortwave cloud radiative effect (SWCRE) is negative, approximately −0.9 °C month^{-1}, indicating that clouds reduce shortwave energy input relative to clear-sky conditions. Cloud shading and latent cooling therefore reduce surface warming, but the net surface-flux tendency remains positive. The weaker net surface warming in the eddy-resolving configuration relative to ERA5 may contribute to the residual coastal cold bias.

Clouds therefore remain an important part of the coastal state. The eddy-resolving ICON configuration has cloud-cover and SWCRE spatial patterns closer to the satellite references than the coarser configuration, indicating an improved cloud-radiative state. Coastal-band cloud cover is approximately 76.7% in the eddy-resolving configuration, approximately 65.0% in the coarser configuration, and approximately 74.8% in MODIS. These cloud and surface-flux diagnostics indicate that marine clouds modulate the air–sea heat exchange and the strength of surface damping, while the leading contrast between the two ICON configurations in the coastal heat balance arises from mean ocean dynamical cooling.

Together, the surface-flux and cloud diagnostics complement the ocean dynamical interpretation. A realistic eastern Pacific climate requires both credible marine cloud radiative effects and credible coastal ocean dynamics. In the eddy-resolving ICON simulation, the coastal cold state is maintained in the presence of positive net surface heating, which identifies mean ocean dynamical cooling as the sustaining process and surface fluxes as damping and modulation terms.

2.7 Coastal-band bias process summary

Figure 7 summarizes the 0–200 km coastal-band diagnostics and places the ICON comparison within the CMIP6 distribution and alongside IFS-FESOM2-SR. The coarser ICON configuration has a coastal SST bias of approximately +2.39 °C and lies on the warm side of the CMIP6 distribution. The eddy-resolving ICON simulation shifts to approximately −0.67 °C, while IFS-FESOM2-SR also produces a pronounced coastal cold bias; both high-resolution simulations lie well beyond the cold side of the CMIP6 distribution. The eddy-resolving ICON simulation and IFS-FESOM2-SR also produce stronger upwelling-favorable wind stress and 50 m upwelling than the coarser ICON configuration. Their upper-ocean current speeds are close to ORAS5, indicating that the improved mean coastal state is associated with a stronger and more realistic wind–upwelling–current response.

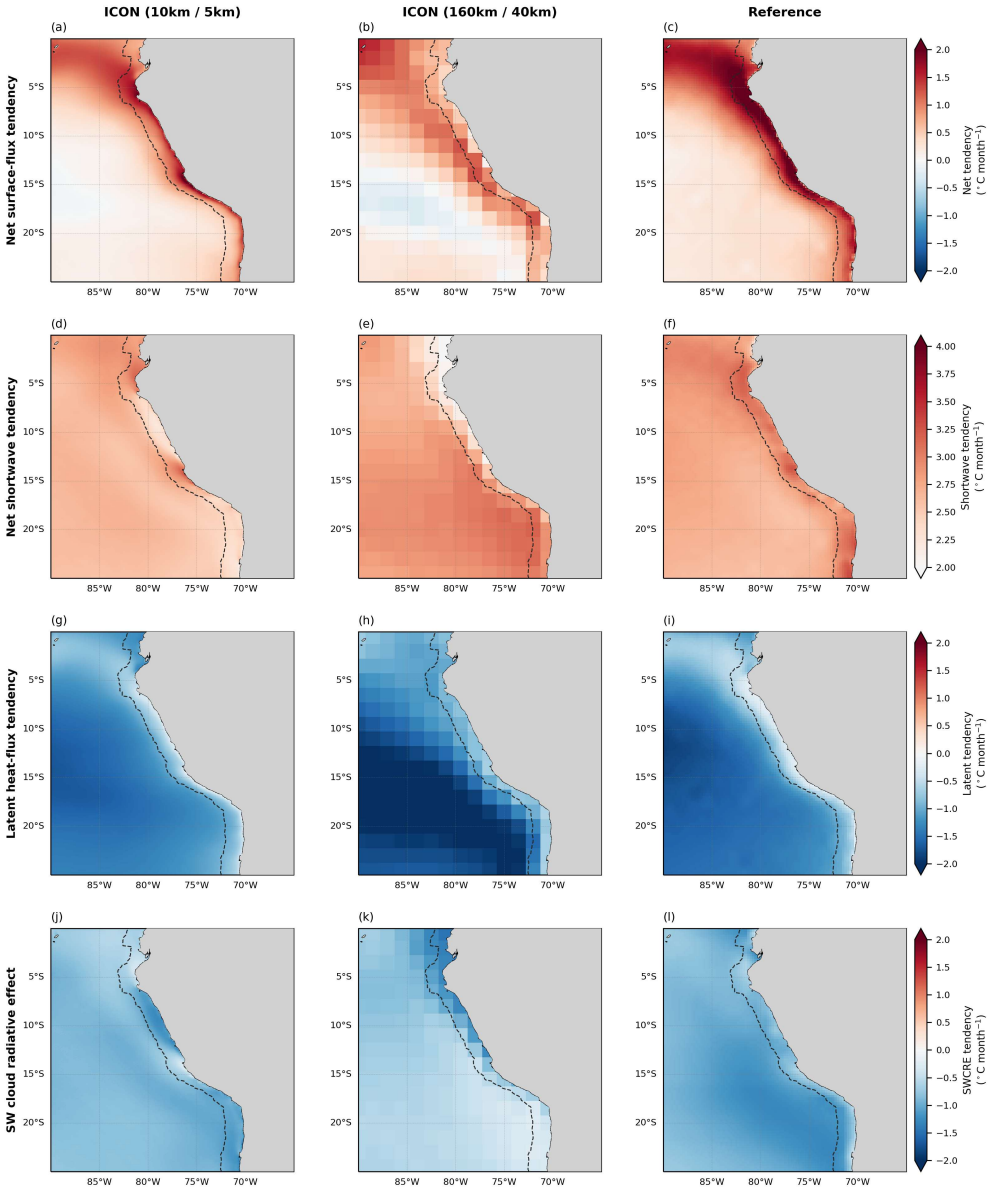

Figure 6: **Surface-flux tendencies and shortwave cloud radiative effect in the Peru coastal upwelling band.** Model columns show ICON (10 km / 5 km) and ICON (160 km / 40 km). Panels show equivalent temperature tendencies for a fixed 0–50 m upper-ocean layer. Rows show net surface-flux tendency, net shortwave tendency, latent heat-flux tendency, and surface shortwave cloud radiative effect (SWCRE). The reference column uses ERA5 for the first three rows and CERES-EBAF for SWCRE. Positive tendencies warm the fixed 0–50 m layer, and negative tendencies cool it.

The tendency diagnostics identify mean ocean dynamics as the common cooling pathway in the eddy-resolving ICON simulation and IFS-FESOM2-SR. Both simulations occupy the strong-cooling side of the CMIP6 distribution for total mean dynamical tendency, with substantial contributions from cross-shore advection and the vertical upwelling tendency. The coarser ICON configuration exhibits much weaker total dynamical cooling. The independent IFS-FESOM2-SR result therefore indicates that strong coastal dynamical cooling is not unique to the eddy-resolving ICON configuration. The transient diagnostics are less uniform: IFS-FESOM2-SR shows a comparatively strong positive total transient tendency, driven mainly by cross-shore transient convergence, whereas the eddy-resolving ICON simulation remains closer to the lower part of the CMIP6 range. This spread reinforces the interpretation that transient heat-flux convergence is model dependent and primarily redistributes heat around the mean coastal cooling pathway.

Net surface-flux tendency remains positive in both ICON configurations, IFS-FESOM2-SR, the reference estimate, and most of the CMIP6 distribution. Surface exchange therefore warms the fixed 0–50 m layer across these comparisons rather than supplying the coastal cooling. Overall, Fig. 7 supports a coherent pathway in which stronger coastal forcing enhances nearshore upwelling and mean ocean dynamical cooling. The similar response in IFS-FESOM2-SR shows that this pathway also appears in an independent high-resolution coupled model, while the differences in transient convergence demonstrate that not every component of the coastal heat budget responds uniformly across models.

3 Discussion

The sign of the coastal heat balance provides the central physical constraint on the interpretation. In the eddy-resolving ICON simulation, positive shortwave heating exceeds the cooling contributions from latent heat loss and cloud shortwave shading in the coastal-band mean, leaving a positive net surface heat input into the fixed 0–50 m layer. Surface exchange therefore tends to warm the cold coastal ocean and damp its SST anomaly rather than generate the cooling. Maintaining a climatologically cold coastal state against this surface warming requires oceanic heat export or a supply of colder water that offsets the positive surface input. The coherent negative tendency from the mean circulation provides this balancing cooling and is therefore the principal sustaining pathway. This heat-balance constraint distinguishes the mechanism of the SST-bias reduction from explanations based primarily on reduced radiative heating or enhanced turbulent heat loss.

The diagnosed pathway links the atmospheric and oceanic coastal responses: sharper representation of the Andes and coastline supports stronger, more coastally confined upwelling-favorable wind stress; the resulting offshore Ekman transport promotes nearshore upwelling; and the associated current structure produces cross-shore and vertical advective cooling of the upper ocean. Previous studies have established the sensitivity of eastern-boundary SST to coastal winds, topography, clouds, upwelling, and the balance among radiation, turbulent exchange, entrainment, and advection[9,10,13,14,20–23]. The present analysis connects these elements within one process budget and identifies mean ocean dynamical cooling as the link between improved coastal forcing and the SST response.

The multimodel context indicates that this association is broader than the comparison between the



Figure 7: **Coastal-band process summary with the CMIP6 distribution and IFS-FESOM2-SR comparison.** Symbols show 1982–2014 means within the Peru coastal band, defined as ocean cells 0–200 km offshore between 25°S and the equator, for the eddy-resolving ICON simulation [ICON (10 km / 5 km)], the coarser ICON configuration [ICON (160 km / 40 km)], observational or reanalysis references, the CMIP6 distribution, and IFS-FESOM2-SR. Purple boxes show the distribution across 43 CMIP6 models (listed in Supplementary Table 1), augmented by the corresponding ICON (160 km / 40 km) value where available; this configuration is also plotted separately to identify its position within each distribution. Boxes span the interquartile range, central lines indicate the median, and whiskers indicate the 5th–95th percentiles. Green crosses show IFS-FESOM2-SR, an independent HighResMIP2 simulation. IFS-NEMO simulations are not shown because their ocean velocity fields were not available in the online archive used for this analysis. Panels summarize (a) SST bias, upwelling-favorable meridional wind stress, 50 m upwelling, and upper-ocean current speed; (b) alongshore, cross-shore, vertical, and total mean dynamical tendencies; (c) monthly transient heat-flux tendencies; and (d) surface-flux and cloud-cover diagnostics. Reference products are OISST for SST, ERA5 for winds and surface-flux terms, ORAS5 for ocean currents, upwelling, and heat-budget terms, CERES-EBAF for SWCRE, and MODIS Aqua+Terra for cloud cover.

two ICON configurations. The eddy-resolving ICON simulation lies on the cold, strongly upwelling and strongly cooling side of the CMIP6 distributions, and IFS-FESOM2-SR independently combines a cold coastal SST state with enhanced upwelling and strong mean dynamical cooling. The two HighResMIP2 simulations differ in several other heat-budget terms, but they share the same mean coastal dynamical pathway. This agreement provides positive evidence that sufficiently resolved coastal forcing and ocean circulation can restore a cooling process that is systematically weak in many coarser coupled models.

Using the same eddy-resolving ICON simulation, Kang et al.[19] found a more realistic southeastern tropical Pacific SST cooling trend than in CMIP6 models and linked the regional cooling to Southern Ocean dynamical cooling and an equatorward teleconnection amplified by subtropical cloud feedback. To examine whether the reduced climatological warm SST bias in the southeastern tropical Pacific is associated with a more realistic cooling trend in the eddy-resolving ICON simulation, we compare regional-mean SST trends in Supplementary Fig. 5. These regional means provide a complementary diagnostic: they average over the full eastern Pacific study region or the narrow Peru coastal band. In these area means, ERSSTv5 and the eddy-resolving ICON simulation show weak trends over 1979–2014, whereas the coarser ICON configuration warms significantly in both regions. The differences in historical SST trends between the two ICON configurations, and among the CMIP6, HighResMIP1, and HighResMIP2 multimodel means, are much smaller than the corresponding differences in SST climatology. The two analyses are therefore complementary rather than contradictory: the climatological mean-state improvement is linked most directly to the local coastal topography–wind–upwelling–current–advection pathway, whereas regional historical trends also reflect time-dependent forcing, internal variability, spatial cancellation, and remote ocean–cloud influences.

Although mean ocean dynamics cool the coastal ocean, other processes partly offset this cooling and help determine the resulting SST. Net surface-flux tendencies remain positive, so surface exchange damps the dynamically generated cold state rather than producing it. Marine clouds regulate the strength of this damping through shortwave cloud radiative effects, while latent heat loss provides an additional cooling contribution. The improved cloud-cover and SWCRE structure in the eddy-resolving ICON configuration is therefore important for the coupled equilibrium, but it modulates a coastal state sustained primarily by ocean dynamics. This interpretation is consistent with the established role of southeast Pacific stratocumulus in controlling shortwave input and boundary-layer stability[4,6,11,12].

Monthly transient heat-flux convergence also modifies the coastal heat balance, but its patchy, sign-changing spatial pattern and larger intermodel spread distinguish it from the coherent mean cooling. Mesoscale eddies, filaments, and fronts redistribute heat between the nearshore upwelling zone and offshore waters[15–18,24,25]. The strong positive transient tendency in IFS-FESOM2-SR, compared with the weaker tendency in the eddy-resolving ICON simulation, indicates that transient heat redistribution can differ substantially even when models share strong upwelling and mean dynamical cooling. The mean dynamical pathway is therefore the more robust response across models, whereas transient transport remains model dependent.

This distinction also helps interpret the emerging transition from the traditional coastal warm bias in lower-resolution and CMIP6 models toward a residual or excessive cold bias in HighResMIP2. The eddy-resolving ICON configuration restores the cooling pathway, but its stronger-than-reference upwelling and mean dynamical cooling are consistent with the remaining modest cold

bias. High resolution therefore changes the central modelling problem: the priority is no longer only to generate sufficient coastal cooling, but also to balance its magnitude against surface-flux damping and transient heat redistribution. Accurate simulation therefore requires both a realistic mean coastal dynamical cooling pathway and a realistic balance of the surface-flux and transient tendencies that offset or redistribute this cooling.

The progressive SST-bias reduction from CMIP6 to HighResMIP1 and HighResMIP2 demonstrates the broader value of high-resolution Earth system modelling for narrow coastal regimes that are poorly represented on conventional grids. Although the affected coastal region occupies a small area, its climatic influence is potentially much wider. Peru coastal SST helps organize lower-tropospheric stability, southeast Pacific cloud cover and precipitation, and the zonal SST gradients connected to the equatorial cold tongue and tropical Pacific circulation. The accompanying reduction of the coastal precipitation bias is consistent with this wider coupled adjustment. These local and basin-scale pathways complement high-resolution studies emphasizing terrain-related cloud–wind effects, tropical Pacific adjustments, and eddy or cloud feedbacks[9,19].

The main limitation of this study is that the two ICON configurations differ in atmospheric formulation, physical parameterizations, and atmospheric and oceanic grid resolution; their contrast therefore reflects configuration- and grid-resolution-related differences rather than a controlled grid-resolution-only experiment. Nevertheless, the progression across CMIP6 and HighResMIP ensembles, together with the independent IFS-FESOM2-SR result, supports a grid-resolution-linked interpretation of the coastal response. The fixed 0–50 m layer provides a consistent comparison depth but neither represents the local mixed layer everywhere nor closes the complete upper-ocean heat budget. The advection and upwelling tendencies are primarily diagnosed offline from archived monthly fields rather than accumulated online at every model time step. Consequently, time-varying diffusion and mixing cannot be reconstructed explicitly. Online heat budget diagnostics, even for representative shorter periods, would provide a more complete assessment of diffusion, advection, and transient redistribution[26].

Future work should separate atmospheric resolution, ocean resolution, coastal topography, and model-physics effects through controlled sensitivity experiments; apply harmonized heat-budget diagnostics across models and output frequencies; and extend the analysis to additional HighResMIP2 simulations and ensembles. Such tests will determine how accurately the restored cooling is balanced by surface fluxes and transient heat redistribution and how its regional benefits propagate into the tropical Pacific. The central physical advance is the identification of a resolved coastal topography–wind–upwelling–current–advection pathway that sustains the Peru cold state against positive surface heating and provides a generalizable basis for reducing eastern Pacific coastal SST bias.

4 Conclusions

This study diagnoses why the eddy-resolving ICON simulation produced within the EERIE framework reduces the strong Peru coastal warm SST bias present in the coarser ICON configuration and common in the CMIP6 multimodel mean, while leaving a modest residual cold bias in the coastal-band mean. The expanded SST-bias comparison further shows that the Peru coastal warm bias

decreases progressively with increasing model resolution, from CMIP6 to HighResMIP1 and HighResMIP2. A parallel precipitation comparison shows a reduction of the coastal wet bias, which is nearly absent in the eddy-resolving ICON simulation. Using a common 0–200 km Peru coastal band and process-oriented diagnostics for winds, upwelling, currents, mean ocean dynamical tendencies, monthly transient heat-flux convergence, surface fluxes, and clouds, we show that the SST-bias reduction is concentrated in the narrow coastal upwelling zone and is organized around a restored coastal dynamical pathway. CMIP6 process distributions and the independent IFS-FESOM2-SR comparison provide additional context for this pathway.

The key process chain begins with an improved representation of the Andes, coastline, and nearshore wind field in the eddy-resolving ICON configuration. Sharper coastal geometry and orography are associated with stronger, coastally confined upwelling-favorable wind stress. This enhanced coastal forcing strengthens nearshore upwelling and supports a more realistic coastally confined Peru Current structure. The resulting mean ocean dynamical tendency provides coherent cooling of the fixed 0–50 m upper-ocean layer, mainly through cross-shore advection and the 50 m vertical upwelling tendency. IFS-FESOM2-SR independently exhibits strong upwelling and mean dynamical cooling on the cold side of the CMIP6 distributions, showing that the central pathway is not restricted to the eddy-resolving ICON simulation. Upwelling and total mean dynamical cooling in the eddy-resolving configuration are stronger than the ORAS5-based estimates, consistent with its modest coastal cold bias and an apparent over-intensification of the restored pathway.

Monthly transient heat-flux convergence, surface fluxes, and clouds are active parts of the coupled coastal heat balance, but they mainly modulate the dynamically cooled state. Monthly transient tendencies are patchy and sign-changing, indicating heat redistribution within and across the coastal transition zone around the organized nearshore cooling pathway supplied by the mean circulation. Net surface-flux tendency is positive in the coastal-band mean in both ICON configurations, so surface exchange warms the fixed 0–50 m layer and damps the cold coastal state. The eddy-resolving configuration also improves cloud-cover structure and SWCRE relative to the coarser configuration. These cloud and surface-flux changes modulate the damping environment, while mean coastal dynamical cooling remains the primary process explaining the SST-bias reduction between the two ICON configurations.

Overall, the results show that resolving the coupled topography–wind–upwelling–current–advection pathway is central to reducing the Peru coastal SST warm bias in coupled ICON configurations. The improvement reflects a localized restoration of coastal ocean dynamics that allows the upwelling system to maintain cold SST against positive net surface heating. The broader comparison from CMIP6 to HighResMIP1 and HighResMIP2 places the response of the eddy-resolving ICON simulation in a wider high-resolution modelling context, showing that the Peru coastal warm bias is progressively reduced with increasing model resolution. This mechanism provides a process-based explanation for the improved eastern Pacific coastal climate state in the eddy-resolving ICON simulation and highlights the importance of representing both atmospheric coastal forcing and oceanic nearshore dynamics in high-resolution climate models.

5 Methods

5.1 Model simulations and reference products

We compare two coupled ICON configurations. The first is an eddy-resolving ICON simulation with nominal grid spacings of approximately 10 km in the atmosphere and 5 km in the ocean. This simulation follows the Sapphire configuration described by Hohenegger et al.[27] and represents the high-resolution ICON contribution used in the EERIE/HighResMIP2 archive[28]. The eddy-resolving ICON configuration couples the ICON atmosphere, ICON ocean, and JSBACH land component. Its atmosphere uses the native R2B08 unstructured grid and its ocean uses the native R2B09 unstructured grid, equivalent to about 0.09° and 0.045° in the tropics, respectively. At these grid spacings, the ocean resolves much of the mesoscale circulation in the Peru coastal transition zone, while the atmosphere more accurately represents the steep Andes, coastline, and associated nearshore wind gradients. Hereafter, "high resolution" refers to finer horizontal model-grid spacing unless otherwise specified.

The second is a coarser ICON configuration with nominal grid spacings of approximately 160 km in the atmosphere and 40 km in the ocean. It couples the numerical-weather-prediction formulation of the ICON atmosphere with the ICON ocean and JSBACH land component. Its atmosphere uses the native R2B04 unstructured grid, equivalent to about 1.4°, and its ocean uses the native R2B06 unstructured grid, equivalent to about 0.36°[29–31]. Unless otherwise noted, analyses of both configurations use historically forced simulations over the common period 1982–2014. Table 1 summarizes the source grids and approximate resolutions of all model and reference products.

To place the two ICON configurations in a broader model context, the SST-bias comparison in Fig. 1 and coastal-band process summary in Fig. 7 also include the CMIP6 historical multimodel mean, the HighResMIP1 and HighResMIP2 multimodel means, and MPI-ESM1-2-XR and IFS-FESOM2-SR as individual high-resolution comparisons[32–34]. The CMIP6 and HighResMIP1 means comprise 43 and 17 historical simulations, respectively. The HighResMIP2 mean comprises four simulations from the EERIE/HighResMIP archive: the eddy-resolving ICON simulation, IFS-FESOM2-SR, IFS-NEMO-ER, and IFS-NEMO-HR[28]. These model groups and individual fields are listed in Supplementary Table 1. They provide context for the progressive reduction of the Peru coastal SST bias across increasingly high-resolution coupled simulations. Because the HighResMIP2 sample contains only four models, it serves as contextual evidence rather than a statistically robust multimodel benchmark. MPI-ESM1-2-XR belongs to the MPI-ESM1.2 HighResMIP family and uses a different atmospheric formulation and ocean grid from the eddy-resolving ICON configuration[34,35].

Reference products are chosen separately for SST, precipitation, atmospheric forcing, ocean circulation, and cloud-radiative diagnostics. Observed SST is taken from NOAA OISST on a 0.25° regular longitude–latitude grid[36,37]. Observed precipitation is taken from the monthly GPCP Version 2.3 product on a 2.5° grid[38]. Atmospheric 10 m winds, wind stress, and surface turbulent and radiative fluxes are evaluated against ERA5 on a 0.25° regular or remapped grid[39]. Ocean currents and vertical velocity are compared with ORAS5 on the ORCA025 curvilinear grid, with an approximate horizontal resolution of 0.25°[40]. ORAS5 vertical velocity at 50 m is diagnosed from horizontal current divergence integrated from the surface to approximately 50 m using the

ORCA025 mesh metrics. OISST, GPCP, ERA5, and ORAS5 use the main 1982–2014 analysis period.

Cloud-radiative and cloud-cover diagnostics use shorter satellite-era reference periods. Shortwave cloud radiative effect (SWCRE) is evaluated against CERES-EBAF on a 1° regular longitude–latitude grid[41,42]. The CERES SWCRE diagnostics use March 2000–March 2013, constrained by the processed CERES-EBAF record. Cloud cover is compared with MODIS Aqua+Terra cloud products on a 1° grid[43]. The MODIS cloud-cover reference is based on daily Aqua+Terra products averaged over 2003–2014. Because these satellite periods are shorter than the full 1982–2014 SST, wind, ocean, and surface-flux analysis periods, they provide satellite-era reference constraints for interpreting the cloud-radiative state.

Most diagnostics from the two ICON configurations are computed before interpolation, using native-grid or highest-available source fields. The display grid used in a figure is therefore not always the native analysis grid. Model and reference fields are first averaged in time on their native or source grids where possible, then interpolated to regular grids for plotting and, where required, regional diagnostics. SST bias panels are compared on the OISST 0.25° reference grid, and precipitation panels are compared on the GPCP 2.5° reference grid after time averaging. Wind and surface-flux diagnostics are displayed on atmosphere-based grids, while ocean-current, upwelling, and heat-budget diagnostics are displayed on ocean-based grids. Atmospheric fields from the eddy-resolving configuration are generally displayed on 0.10° grids and ocean fields on 0.05°–0.10° grids, depending on the diagnostic. Atmospheric and ocean fields from the coarser configuration are displayed on approximately 1.5° and 0.4° grids, respectively. ORAS5 and ERA5 are displayed on 0.25° regular grids; CERES SWCRE is interpolated to the ERA5-style display grid for comparison with surface-flux diagnostics. Figure-specific display and analysis grids are reported in Supplementary Table 2.

All model and reference fields are converted to common physical units before regional averaging and tendency calculations. The main SST, wind, ocean-current, heat-budget, surface-flux, and cloud diagnostics are based on monthly mean model and reference fields, or on monthly mean product fields where available. Climatological means and tendencies are computed from these monthly fields over the stated analysis periods, with monthly means weighted by the number of days in each month where appropriate. Biases are computed relative to the corresponding reference product after applying consistent temporal averaging and spatial masking. For process summaries, all quantities are averaged over the Peru coastal upwelling band defined below.

5.2 Coastal band definition

The Peru coastal upwelling band is defined separately on each model or reference grid as ocean grid cells whose centers lie within 0–200 km of the South American coastline between 25°S and 0°. This band is used consistently for the process diagnostics and coastal-band summaries in Figs. 3–7. The broader map domain is 90°W–65°W and 25°S–0°.

The 0–200 km width is motivated by the reference cross-shore structure of the coastal upwelling system. In particular, the ORAS5 cross-shore profile of vertical velocity at 50 m shown in Fig. 3g indicates that the strongest nearshore upwelling signal is concentrated within the first few hundred kilometers from the coast and weakens offshore. This width is also consistent with the nearshore

Table 1: **Source grids and approximate horizontal resolutions of the model simulations and reference products used in this study.**

Dataset	Source grid	Approximate physical resolution
Eddy-resolving ICON atmosphere	native R2B08 unstructured grid	∼10 km, about 0.09° in the tropics
Eddy-resolving ICON ocean	native R2B09 unstructured grid	∼5 km, about 0.045° in the tropics
Coarser ICON atmosphere	native R2B04 unstructured grid	∼160 km, about 1.4° in the tropics
Coarser ICON ocean	native R2B06 unstructured grid	∼40 km, about 0.36° in the tropics
MPI-ESM1-2-XR atmosphere	ECHAM6.3 T255 atmosphere	∼50 km, about 0.45° in the tropics
MPI-ESM1-2-XR ocean	native TP04 tripolar ocean grid	∼50 km, about 0.45° in the tropics
IFS-FESOM2-SR atmosphere	native Tco639 cubic-octahedral reduced Gaussian grid	∼16–17 km in the Peru region, about 0.15°
IFS-FESOM2-SR ocean	native FESOM2 NG5 unstructured grid	nominally ∼5 km; spatially variable
ORAS5	ORCA025 curvilinear grid	∼0.25°
ERA5	regular/remapped grid	0.25°
NOAA OISST	regular longitude–latitude grid	0.25°
GPCP Version 2.3	regular longitude–latitude grid	2.5°
CMIP6 multimodel mean	preprocessed 1° SST files	1.0°
CERES-EBAF	regular longitude–latitude grid	1.0°
MODIS Aqua+Terra cloud products	1° cloud product grid	1.0°

current and thermal structures shown in Fig. 3. We therefore apply the same 0–200 km coastal band to all model and reference products.

5.3 Mean ocean dynamical tendency diagnostics

Mean upper-ocean dynamical temperature tendencies are diagnosed over a fixed layer of depth $H = 50$ m. This fixed 0–50 m layer provides a common diagnostic layer for comparing all model and reference products consistently. Supplementary Fig. 6 provides annual and seasonal mixed-layer-depth context for the eddy-resolving and coarser ICON configurations and ORAS5. Because the diagnosed layer does not follow the spatially and seasonally varying mixed-layer depth, the tendencies are interpreted as equivalent 0–50 m upper-ocean heat-content tendencies rather than mixed-layer tendencies. We decompose the horizontal velocity into alongshore and cross-shore components, $u_{\parallel}$ and $u_{\perp}$, and decompose the horizontal temperature gradient into derivatives along the coastal coordinate s and cross-shore coordinate n. Alongshore and cross-shore directions are defined from a smoothed South American coastline. The coastline longitude is smoothed with a Gaussian filter before computing the local tangent vector, and the cross-shore normal vector is defined perpendicular to this tangent and oriented offshore. This smoothing reduces grid-scale noise in the coastal-coordinate projection; in the diagnostics used here, a 2° latitude Gaussian smoothing scale is applied. The overbar denotes the analysis-period climatological mean computed

from monthly fields. The alongshore mean advection tendency is

$$A_{\parallel} = -\overline{u}_{\parallel} \frac{\partial \overline{T}}{\partial s}, \tag{1}$$

and the cross-shore mean advection tendency is

$$A_{\perp} = -\overline{u}_{\perp} \frac{\partial \overline{T}}{\partial n}. \tag{2}$$

The vertical upwelling tendency across the base of the layer is approximated as

$$A_z = \frac{\overline{w}_{50}}{H} \left(\overline{T}_{50} - \overline{T}_{0-50} \right), \tag{3}$$

where $\overline{w}_{50}$ is vertical velocity at 50 m, $\overline{T}_{50}$ is temperature at 50 m, and $\overline{T}_{0-50}$ is the 0–50 m mean temperature. This bulk lower-boundary replacement diagnostic is not the local vertical advection term $-\overline{w}\,\partial\overline{T}/\partial z$. Instead, it quantifies the equivalent temperature tendency produced when water at 50 m is exchanged with the overlying fixed-depth layer. The total mean advective and upwelling-related tendency is then

$$A_{\mathrm{mean}} = A_{\parallel} + A_{\perp} + A_z. \tag{4}$$

The sign convention is that negative tendencies cool the 0–50 m layer and positive tendencies warm it. These diagnostics are intended to identify the organized mean dynamical pathways that affect the coastal SST state and to compare their relative contributions across model and reference products. Transient covariance terms are excluded from A_{mean} and are diagnosed separately in the monthly transient heat-flux convergence analysis below.

5.4 Monthly transient heat-flux convergence diagnostics

Monthly transient heat-flux convergence is estimated from velocity–temperature covariance fields following standard eddy heat-transport diagnostics. For a generic velocity component u and temperature T, the transient covariance is defined as

$$\overline{u'T'} = \overline{uT} - \overline{u}\,\overline{T}, \tag{5}$$

with analogous definitions for the meridional and vertical components:

$$\overline{v'T'} = \overline{vT} - \overline{v}\,\overline{T}, \tag{6}$$

$$\overline{w'T'} = \overline{wT} - \overline{w}\,\overline{T}. \tag{7}$$

Here the overbar denotes the average over the analysis period using the available monthly records. For the eddy-resolving ICON configuration, archived monthly product fields such as $\overline{uT}$, $\overline{vT}$, and the corresponding vertical flux products are used where available. These product fields retain the resolved velocity–temperature covariance contained in the archived monthly output. For the coarser ICON configuration and ORAS5, equivalent monthly product fields are not available, so $\overline{uT}$, $\overline{vT}$, and $\overline{wT}$ are estimated from monthly mean velocity and temperature fields. In those cases, the covariance represents monthly velocity–temperature covariability over the analysis period and does not include submonthly covariance.

Projected alongshore and cross-shore components are used to describe how transient covariance aligns with the coastal coordinate system. The alongshore transient convergence is written schematically as

$$A'_{\parallel} = -\frac{\partial \overline{u'_{\parallel} T'}}{\partial s}, \tag{8}$$

and the cross-shore transient convergence as

$$A'_{\perp} = -\frac{\partial \overline{u'_{\perp} T'}}{\partial n}. \tag{9}$$

The vertical transient flux tendency across the base of the 0–50 m layer is approximated as

$$A'_z = \frac{\overline{w'_{50} T'_{50}}}{H}, \tag{10}$$

with the same sign convention as above. The 50 m vertical transient flux tendency represents the transient temperature flux through the base of the fixed 0–50 m layer, while the full vertical divergence of turbulent or mesoscale heat flux lies beyond the scope of this diagnostic.

The total monthly transient tendency is evaluated from the full horizontal divergence of the transient heat flux plus the vertical transient flux tendency,

$$A'_{\mathrm{tot}} = -\nabla_h \cdot \overline{\mathbf{u}'_h T'} + A'_z, \tag{11}$$

and is reported independently of the projected alongshore and cross-shore display components. These diagnostics provide a resolved monthly estimate of transient heat-flux convergence. Higher-frequency variability, unresolved or parameterized mixing, and product-dependent sampling remain part of the residual heat-budget uncertainty.

5.5 Surface-flux and cloud diagnostics

Surface heat fluxes are converted to equivalent 0–50 m temperature tendencies using

$$\overline{A}_Q = \frac{\overline{Q}}{\rho_0 C_p H}, \tag{12}$$

where $\overline{Q}$ is the analysis-period monthly mean net surface heat flux, ρ_0 is a reference seawater density, C_p is the specific heat capacity of seawater, and $H = 50$ m. Positive $\overline{Q}$ is defined downward into the ocean, so positive $\overline{A}_Q$ warms the upper ocean. We apply the same conversion to shortwave and latent heat-flux components when comparing the magnitude of radiative and turbulent contributions. All surface-flux components are converted to a common sign convention before calculating temperature tendencies.

Following the standard cloud radiative effect convention, the surface shortwave cloud radiative effect is defined as the difference between all-sky and clear-sky net surface shortwave radiation[41,42]:

$$\mathrm{SWCRE} = (\mathrm{rsds} - \mathrm{rsus}) - (\mathrm{rsdscs} - \mathrm{rsuscs}), \tag{13}$$

where rsds and rsus are all-sky downwelling and upwelling shortwave radiation at the surface, and rsdscs and rsuscs are the corresponding clear-sky quantities. Negative SWCRE indicates cloud shortwave shading and therefore a reduction of shortwave energy input into the ocean surface. We also examine cloud cover. Where direct low-cloud cover is unavailable, model total cloud cover provides a proxy for marine cloud-cover structure.

Data availability

The eddy-resolving ICON simulation analyzed in this study is the `hist-1950` simulation from the EERIE v20240618 archive, where the historical configuration identifier is ICON-ESM-ER. The HighResMIP2 simulations used in Fig. 1 and Supplementary Fig. 1, together with the native IFS-FESOM2-SR fields used in Fig. 7, are from the EERIE/HighResMIP archive. General information on the EERIE project is available at `https://eerie-project.eu/`. EERIE data are searchable through the ESGF MetaGrid portal at `https://esgf-metagrid.cloud.dkrz.de/search?project=EERIE`. The coarser ICON configuration is documented under the official ICON XPP configuration name in the cited publications[29–31]; supporting materials are archived with DOI `https://doi.org/10.17617/3.UUIIZ8`, and ICON Release 2024.07 is archived with DOI `https://doi.org/10.35089/WDCC/IconRelease2024.07`. The CMIP6 historical simulations and HighResMIP simulations, including MPI-ESM1-2-XR and IFS-FESOM2-SR, are available through the CMIP6/HighResMIP archive and are searchable through the ESGF MetaGrid portal at `https://esgf-metagrid.cloud.dkrz.de/search?project=CMIP6`. The reference products are publicly available from their respective data providers: NOAA OISST at `https://psl.noaa.gov/data/gridded/data.noaa.oisst.v2.highres.html`, GPCP Version 2.3 at `https://psl.noaa.gov/data/gridded/data.gpcp.html`, ERA5 monthly single-level and pressure-level data at `https://cds.climate.copernicus.eu/`, ORAS5 at `https://cds.climate.copernicus.eu/datasets/reanalysis-oras5?tab=download`, CERES-EBAF at `https://ceres.larc.nasa.gov/data/`, and MODIS data at `https://modis.gsfc.nasa.gov/data/`. The processed diagnostics and analysis scripts used to generate the figures are available from the corresponding author upon reasonable request.

Acknowledgements

We thank Dian Putrasahan, Jürgen Kröger, Helmuth Haak, and Jin-Song von Storch for preparing the model simulations and Fabian Wachsmann and Chathu Wickramage for cataloguing the data. We also acknowledge support from the European Eddy-Rich Earth System Models (EERIE) project (`https://cordis.europa.eu/project/id/101081383`). This study was funded by the European Union's Horizon Europe programme through ASPECT (WM and DY; grant no. 101081460) and by the German Federal Ministry of Education and Research (BMBF) through the Coming Decade project (WM and DY; grant no. 01LP2327E). We acknowledge the German Climate Computing Center (DKRZ) for providing computational resources. We thank Dr. Lin Lin at the Max Planck Institute for Meteorology for the careful and constructive assessment of this manuscript.

References

[1] Penven, P., Echevin, V., Pasapera, J., Colas, F. & Tam, J. Average circulation, seasonal cycle, and mesoscale dynamics of the peru current system: A modeling approach. *Journal of Geophysical Research* **110**, C10021 (2005).

[2] Chavez, F. P., Bertrand, A., Guevara-Carrasco, R., Soler, P. & Csirke, J. The northern humboldt current system: Brief history, present status and a view towards the future. *Progress in Oceanography* **79**, 95–105 (2008).

[3] Montecino, V. & Lange, C. B. The humboldt current system: Ecosystem components and processes, fisheries, and sediment studies. *Progress in Oceanography* **83**, 65–79 (2009).

[4] Stevens, B. *et al.* Evaluation of large-eddy simulations via observations of nocturnal marine stratocumulus. *Monthly Weather Review* **133**, 1443–1462 (2005).

[5] Wood, R. *et al.* The vamos ocean-cloud-atmosphere-land study regional experiment (vocals-rex): Goals, platforms, and field operations. *Atmospheric Chemistry and Physics* **11**, 627–654 (2011).

[6] Zuidema, P. *et al.* Challenges and prospects for reducing coupled climate model sst biases in the eastern tropical atlantic and pacific oceans. *Bulletin of the American Meteorological Society* **97**, 2305–2328 (2016).

[7] Mechoso, C. R. *et al.* The seasonal cycle over the tropical pacific in coupled ocean–atmosphere general circulation models. *Monthly Weather Review* **123**, 2825–2838 (1995).

[8] de Szoeke, S. P. & Xie, S.-P. The tropical eastern pacific seasonal cycle: Assessment of errors and mechanisms in ipcc ar4 coupled ocean–atmosphere general circulation models. *Journal of Climate* **21**, 2573–2590 (2008).

[9] Dong, E. *et al.* The process-oriented understanding on the reduced double-itcz bias in the high-resolution cesm1. *Geophysical Research Letters* **52**, e2024GL112087 (2025).

[10] Meegan-Kumar, D. *et al.* Optimizing topographic boundary conditions for east pacific climate simulation. *Journal of Climate* **38**, 2497–2524 (2025).

[11] Sun, R., Moorthi, S., Xiao, H. & Mechoso, C. R. Simulation of low clouds in the southeast pacific by the ncep gfs: Sensitivity to vertical mixing. *Atmospheric Chemistry and Physics* **10**, 12261–12272 (2010).

[12] Wyant, M. C. *et al.* The prevoca experiment: Modeling the lower troposphere in the southeast pacific. *Atmospheric Chemistry and Physics* **10**, 4757–4774 (2010).

[13] Small, R. J., Curchitser, E., Hedstrom, K., Kauffman, B. & Large, W. G. The benguela upwelling system: Quantifying the sensitivity to resolution and coastal wind representation in a global climate model. *Journal of Climate* **28**, 9409–9432 (2015).

[14] Baldwin, J. W., Atwood, A. R., Vecchi, G. A. & Battisti, D. S. Outsize influence of central american orography on global climate. *AGU Advances* **2**, e2020AV000343 (2021).

[15] Chaigneau, A., Gizolme, A. & Grados, C. Mesoscale eddies off peru in altimeter records: Identification algorithms and eddy spatio-temporal patterns. *Progress in Oceanography* **79**, 106–119 (2008).

[16] Toniazzo, T., Mechoso, C. R., Shaffrey, L. C. & Slingo, J. M. Upper-ocean heat budget and ocean eddy transport in the south-east pacific in a high-resolution coupled model. *Climate Dynamics* **35**, 1309–1329 (2010).

[17] Colas, F., McWilliams, J. C., Capet, X. & Kurian, J. Heat balance and eddies in the peru-chile current system. *Climate Dynamics* **39**, 509–529 (2012).

[18] Colas, F., Capet, X., McWilliams, J. C. & Li, Z. Mesoscale eddy buoyancy flux and eddy-induced circulation in eastern boundary currents. *Journal of Physical Oceanography* **43**, 1073–1095 (2013).

[19] Kang, S. M. *et al.* Km-scale coupled simulation and model–observation sst trend discrepancy. *Proceedings of the National Academy of Sciences* **123**, e2522161123 (2026).

[20] Colbo, K. & Weller, R. A. The variability and heat budget of the upper ocean under the chile-peru stratus. *Journal of Marine Research* **65**, 607–637 (2007).

[21] de Szoeke, S. P., Fairall, C. W., Wolfe, D. E., Bariteau, L. & Zuidema, P. Surface flux observations on the southeastern tropical pacific ocean and attribution of sst errors in coupled ocean–atmosphere models. *Journal of Climate* **23**, 4152–4174 (2010).

[22] Zheng, Y. *et al.* Upper-ocean processes under the stratus cloud deck in the southeast pacific ocean. *Journal of Climate* **23**, 4253–4271 (2010).

[23] Holte, J., Straneo, F., Farrar, J. T. & Weller, R. A. Heat and salinity budgets at the stratus mooring in the southeast pacific. *Journal of Geophysical Research: Oceans* **119**, 8162–8179 (2014).

[24] Bishop, S. P., Small, R. J. & Bryan, F. O. The global sink of available potential energy by mesoscale air–sea interaction. *Journal of Advances in Modeling Earth Systems* **12**, e2020MS002118 (2020).

[25] Zhang, Z. *et al.* Submesoscale inverse energy cascade enhances southern ocean eddy heat transport. *Nature Communications* **14**, 1335 (2023).

[26] Gao, G. *et al.* Drivers of marine heatwaves in the east china sea and the south yellow sea in three consecutive summers during 2016–2018. *Journal of Geophysical Research: Oceans* **125**, e2020JC016518 (2020).

[27] Hohenegger, C. *et al.* ICON-Sapphire: simulating the components of the earth system and their interactions at kilometer and subkilometer scales. *Geoscientific Model Development* **16**, 779–811 (2023).

[28] Roberts, M. J. *et al.* High-resolution model intercomparison project phase 2 (HighResMIP2) towards CMIP7. *Geoscientific Model Development* **18**, 1307–1332 (2025).

[29] Müller, W. A. *et al.* ICON: Toward vertically integrated model configurations for numerical weather prediction, climate predictions, and projections. *Bulletin of the American Meteorological Society* E1017–E1031 (2025).

[30] Müller, W. A. *et al.* The ICON-based earth system model for climate predictions and projections (ICON XPP v1.0). *Geoscientific Model Development* **18**, 9385–9415 (2025).

[31] Yu, D., Dommenget, D., Pohlmann, H. & Müller, W. A. A systematic atmospheric parameter optimization method to improve ENSO simulation in the ICON XPP earth system model. *Geoscientific Model Development* **19**, 5531–5552 (2026).

[32] Eyring, V. *et al.* Overview of the coupled model intercomparison project phase 6 (cmip6) experimental design and organization. *Geoscientific Model Development* **9**, 1937–1958 (2016).

[33] Haarsma, R. J. *et al.* High resolution model intercomparison project (highresmip v1.0) for cmip6. *Geoscientific Model Development* **9**, 4185–4208 (2016).

[34] Gutjahr, O. *et al.* Max planck institute earth system model (MPI-ESM1.2) for the high-resolution model intercomparison project (HighResMIP). *Geoscientific Model Development* **12**, 3241–3281 (2019).

[35] Müller, W. A. *et al.* A higher-resolution version of the max planck institute earth system model (MPI-ESM1.2-HR). *Journal of Advances in Modeling Earth Systems* **10**, 1383–1413 (2018).

[36] Reynolds, R. W. *et al.* Daily high-resolution-blended analyses for sea surface temperature. *Journal of Climate* **20**, 5473–5496 (2007).

[37] Banzon, V., Smith, T. M., Chin, T. M., Liu, C. & Hankins, W. A long-term record of blended satellite and in situ sea-surface temperature for climate monitoring, modeling and environmental studies. *Earth System Science Data* **8**, 165–176 (2016).

[38] Adler, R. F. *et al.* The global precipitation climatology project (GPCP) monthly analysis (new version 2.3) and a review of 2017 global precipitation. *Atmosphere* **9**, 138 (2018).

[39] Hersbach, H. *et al.* The era5 global reanalysis. *Quarterly Journal of the Royal Meteorological Society* **146**, 1999–2049 (2020).

[40] Zuo, H., Balmaseda, M. A., Mogensen, K. & Tietsche, S. Ocean5: The ecmwf ocean reanalysis system and its real-time analysis component. Tech. Rep. Technical Memorandum 823, European Centre for Medium-Range Weather Forecasts (2019).

[41] Loeb, N. G. *et al.* Clouds and the earth's radiant energy system (ceres) energy balanced and filled (ebaf) top-of-atmosphere (toa) edition-4.0 data product. *Journal of Climate* **31**, 895–918 (2018).

[42] Kato, S. *et al.* Surface irradiances of edition 4.0 clouds and the earth's radiant energy system energy balanced and filled data product. *Journal of Climate* **31**, 4501–4527 (2018).

[43] Platnick, S. *et al.* The modis cloud optical and microphysical products: Collection 6 updates and examples from terra and aqua. *IEEE Transactions on Geoscience and Remote Sensing* **55**, 502–525 (2017).

Supplementary Tables

Supplementary Table 1: **Model groups used for the SST- and precipitation-bias comparisons in Fig. 1 and Supplementary Fig. 1, and for the multimodel process context in Fig. 7.** SST and precipitation fields are compared with NOAA OISST and GPCP, respectively, over 1982–2014.

Group	Experiment / source	Number	Models
CMIP6 MMM	historical, monthly	43	ACCESS-CM2; ACCESS-ESM1-5; AWI-CM-1-1-MR; AWI-ESM-1-1-LR; BCC-CSM2-MR; BCC-ESM1; CAMS-CSM1-0; CESM2-FV2; CESM2-WACCM; CESM2; CIESM; CMCC-CM2-HR4; CMCC-CM2-SR5; CMCC-ESM2; CanESM5; E3SM-1-1-ECA; E3SM-1-1; EC-Earth3-AerChem; EC-Earth3-CC; EC-Earth3-Veg-LR; EC-Earth3-Veg; EC-Earth3; FGOALS-f3-L; FGOALS-g3; FIO-ESM-2-0; GFDL-CM4; GISS-E2-1-G-CC; GISS-E2-1-G; ICON-ESM-LR; INM-CM4-8; INM-CM5-0; IPSL-CM6A-LR; KIOST-ESM; MIROC6; MPI-ESM-1-2-HAM; MPI-ESM1-2-HR; MPI-ESM1-2-LR; MRI-ESM2-0; NESM3; NorESM2-LM; NorESM2-MM; SAM0-UNICON; TaiESM1
HighResMIP1 MMM	historical, monthly	17	AWI-CM-1-1-HR; AWI-CM-1-1-LR; BCC-CSM2-HR; CMCC-CM2-HR4; CMCC-CM2-VHR4; CNRM-CM6-1; CNRM-CM6-1-HR; EC-Earth3P; EC-Earth3P-HR; ECMWF-IFS-HR; ECMWF-IFS-LR; ECMWF-IFS-MR; HadGEM3-GC31-HH; HadGEM3-GC31-HM; INM-CM5-H; MPI-ESM1-2-HR; MPI-ESM1-2-XR
HighResMIP2 MMM	historical, monthly	4	ICON (10 km / 5 km); IFS-FESOM2-SR; IFS-NEMO-ER; IFS-NEMO-HR
Fig. 1 and Supplementary Fig. 1 subset	historical, monthly	3	ICON (160 km / 40 km); MPI-ESM1-2-XR; ICON (10 km / 5 km)

Supplementary Table 2: **Display and analysis grids used for the main and supplementary figures.** Most diagnostics from ICON (10 km / 5 km) and ICON (160 km / 40 km) are computed from native-grid or highest-available fields before interpolation; the display grid is therefore not always the native analysis grid.

Figure	ICON (10 km / 5 km) shown on	ICON (160 km / 40 km) shown on	Reference shown on
Fig. 1 SST bias	native ocean climatology interpolated to OISST 0.25°	native ocean climatology interpolated to OISST 0.25°	OISST 0.25°; CMIP6, HighResMIP1, HighResMIP2, and MPI-ESM1-2-XR SST climatologies interpolated to OISST 0.25°
Fig. 2 wind/topography	atmosphere 0.10° display	atmosphere 1.50° display	ERA5 0.25°
Fig. 3 currents/upwelling	ocean 0.05° display	ocean 0.40° display	ORAS5 0.25°
Fig. 4 mean dynamical tendency	ocean 0.10° display	ocean 0.40° display	ORAS5 0.25°
Fig. 5 transient heat-flux convergence	ocean 0.10° display	ocean 0.40° display	ORAS5 0.25°
Fig. 6 surface flux/cloud radiative terms	atmosphere 0.10° display	atmosphere 1.50° display	ERA5 0.25° for net/SW/latent; CERES 1.0° for SWCRE, interpolated to ERA5-style display
Fig. 7 process summary	no map grid; coastal-band means from Figs. 1–6 and Fig. 4	same	reference products and CMIP6 distributions; IFS-FESOM2-SR native NG5 ocean diagnostics remapped to a regional 0.10° grid
Fig. 1 precipitation bias	atmosphere climatology interpolated to GPCP 2.5°	atmosphere climatology interpolated to GPCP 2.5°	GPCP 2.5°; multimodel and MPI-ESM1-2-XR fields interpolated to the same grid
Fig. 2 lower-tropospheric meridional wind v	0.25° pressure–latitude cross-section from ICON (10 km / 5 km) pressure-level output	0.25° pressure–latitude cross-section from ICON (160 km / 40 km) pressure-level output	0.25° pressure–latitude cross-section from ERA5 pressure-level output
Fig. 3 daily/monthly transient sensitivity	daily ocean-output grid at 0.25°; monthly native-product diagnostics interpolated to the daily-data grid before differencing	not shown	not shown
Fig. 4 cloud structure	atmosphere 0.10° display	atmosphere 1.50° display	MODIS Aqua+Terra 1.0°
Fig. 5 historical SST evolution and trends	regional means from ICON (10 km / 5 km) ocean SST	regional means from ICON (160 km / 40 km) ocean SST	ERSSTv5 and CMIP6/HighResMIP regional means; no map grid
Fig. 6 mixed-layer depth	published `gr` MLD at 0.25°	ocean 0.40° display	ORAS5 0.25°

Supplementary Figures

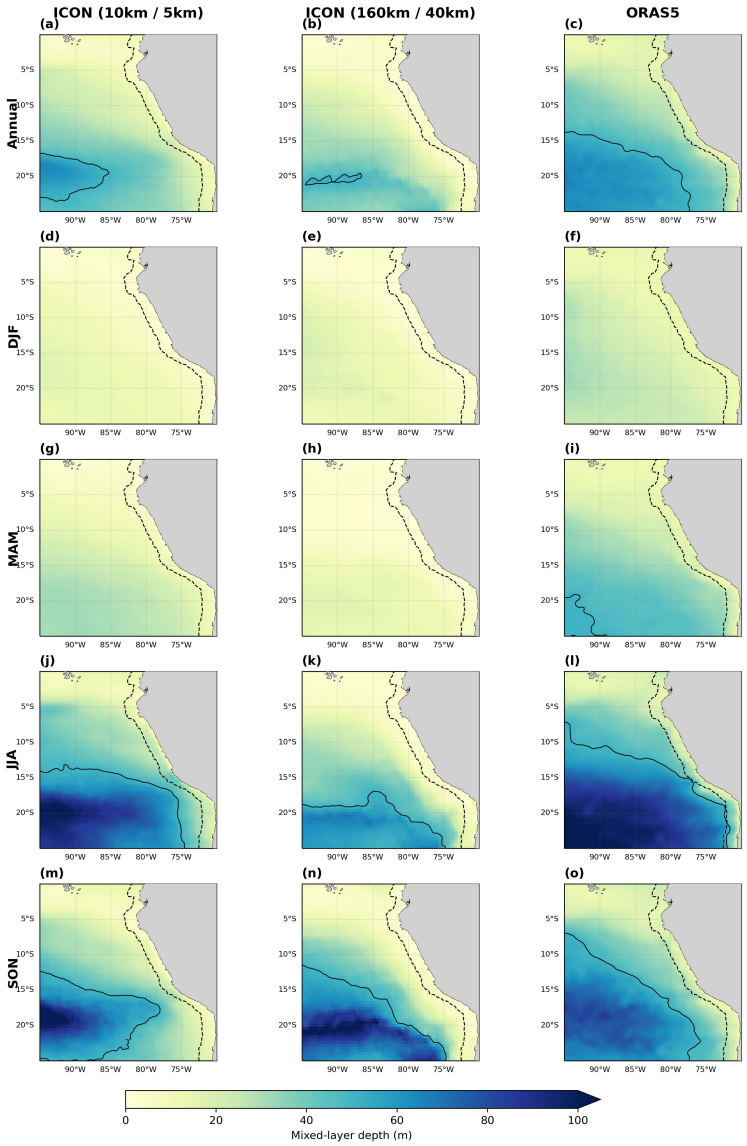

Supplementary Figure 1: **Precipitation climatology and bias.** Panel (a) shows annual-mean precipitation from GPCP over 1982–2014. Panels (b)–(g) show annual-mean precipitation bias relative to GPCP for the CMIP6 multimodel mean, HighResMIP1 multimodel mean, HighResMIP2 multimodel mean, ICON (160 km / 40 km), MPI-ESM1-2-XR, and ICON (10 km / 5 km). Positive values indicate excessive precipitation and negative values indicate deficient precipitation. Labels report the mean bias within the 0–200 km Peru coastal band (coastal bias) and over the full plotted domain (domain bias). The dashed black line marks the offshore edge of the coastal band, which extends from 25°S to the equator.

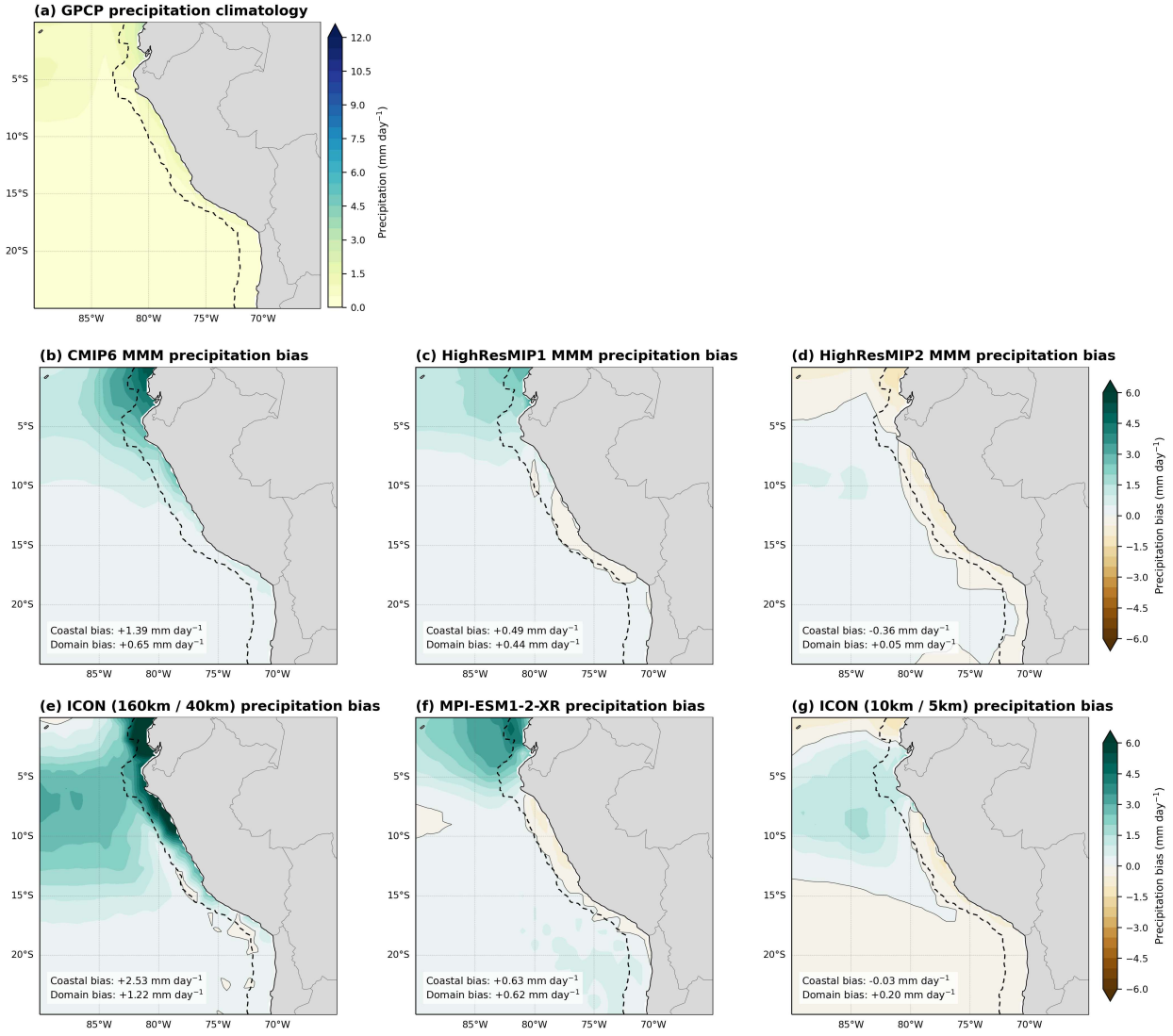

Supplementary Figure 2: **Lower-tropospheric meridional wind structure over the Peru coastal band.** Panels (a)–(c) compare annual-mean pressure–latitude cross-sections of meridional wind in ICON (10 km / 5 km), ICON (160 km / 40 km), and ERA5 over 1982–2014, averaged over ocean cells 0–200 km offshore between 25°S and the equator. Panel (d) shows ICON (10 km / 5 km) minus ICON (160 km / 40 km). The solid black curves show surface meridional wind stress τ_y on the right-hand axis, and the dashed curves in panels (a)–(c) show maximum land orography as a scaled pressure-coordinate reference.

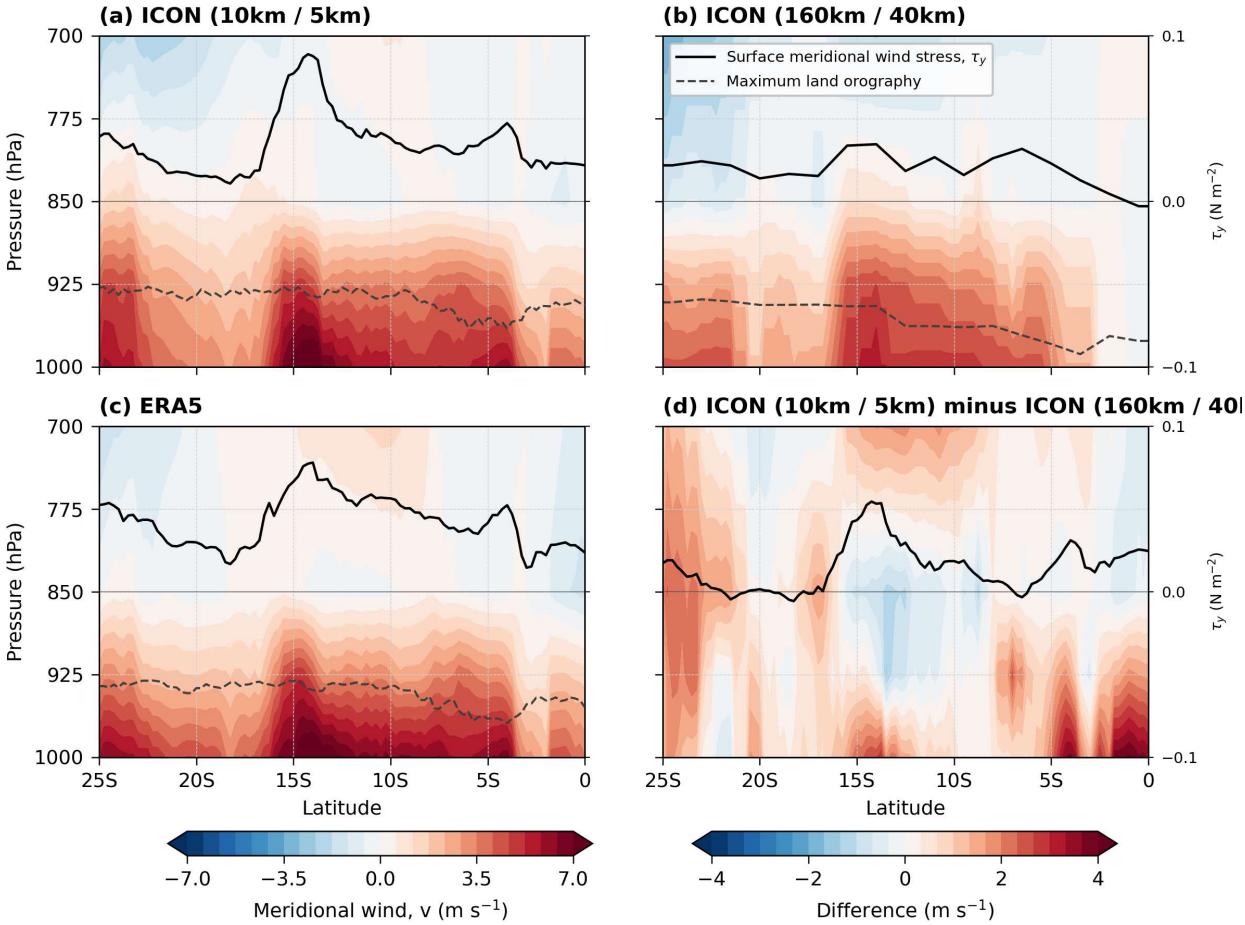

Supplementary Figure 3: **Daily versus monthly transient heat-flux convergence in ICON (10 km / 5 km).** Panels compare annual-mean transient temperature tendency diagnostics for a fixed 0–50 m upper-ocean layer computed from daily ocean output and from monthly native products, together with their difference (daily minus monthly). Rows show alongshore transient heat-flux convergence, cross-shore transient heat-flux convergence, the 50 m vertical transient flux tendency, and the total transient tendency. Negative values indicate cooling and positive values indicate warming. The dashed line marks the 200 km offshore boundary of the Peru coastal upwelling band defined in Fig. 3. Daily fields are displayed on the 0.25° grid, and monthly native-product fields are interpolated to this daily-data grid before differencing.

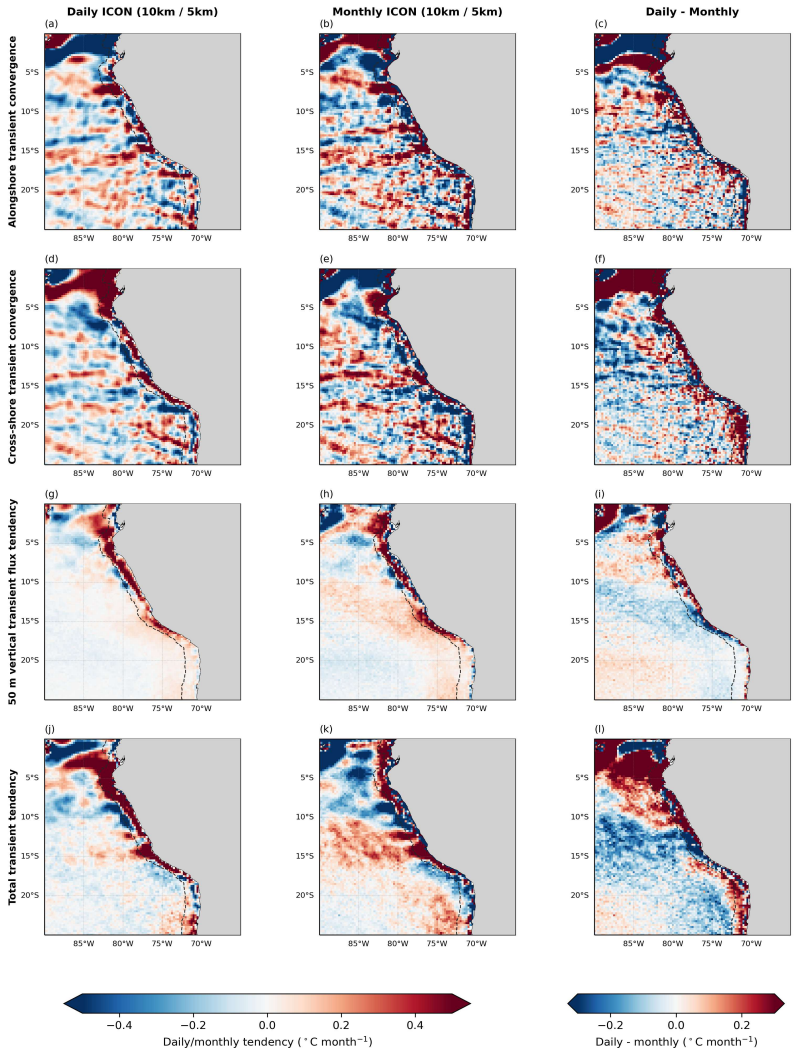

Supplementary Figure 4: **Cloud-cover structure in the southeast Pacific.** Panels compare annual-mean cloud cover in ICON (10 km / 5 km), ICON (160 km / 40 km), and the MODIS satellite reference. Model total cloud cover is used as a marine cloud-cover proxy where direct low-cloud cover is unavailable. The dashed black line marks the offshore edge of the 0–200 km Peru coastal band.

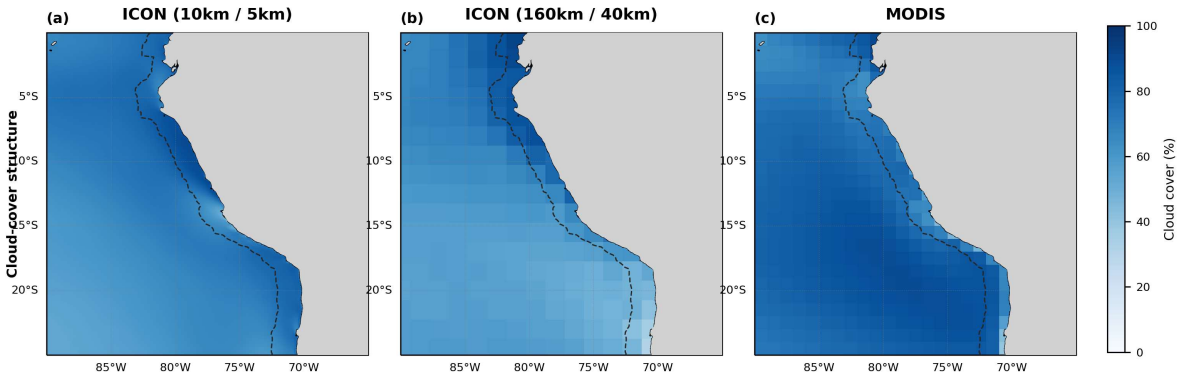

Supplementary Figure 5: **Historical SST evolution and linear trends over 1979–2014 in the eastern Pacific study region and Peru coastal band.** Panels (a) and (b) compare ICON (10 km / 5 km), ICON (160 km / 40 km), and ERSSTv5 over the full study region (90°W–65°W, 25°S–0°) and the 0–200 km Peru coastal band, respectively. Panels (c) and (d) compare the CMIP6, HighResMIP1, and HighResMIP2 multimodel means with ERSSTv5 over the same regions. Thin curves show monthly SST, thick curves show the smoothed SST evolution, and dashed horizontal lines indicate the corresponding period means. Legend values report linear trends estimated from deseasonalized monthly SST, expressed as the trend plus or minus the half-width of the autocorrelation-adjusted approximate 95% confidence interval. For the multimodel means, the uncertainty describes the temporal trend of the multimodel-mean time series rather than intermodel spread.

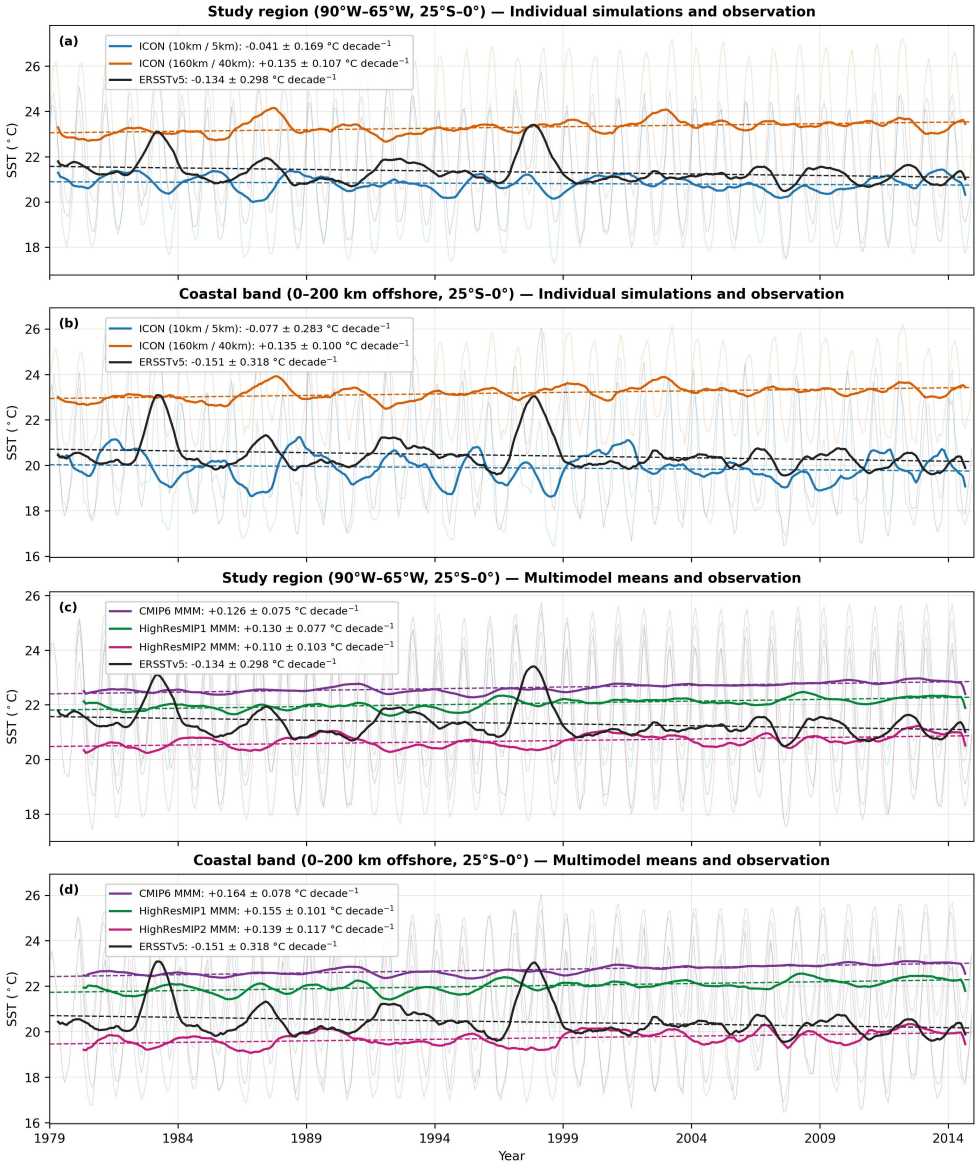

Supplementary Figure 6: **Annual and seasonal mixed-layer depth in the Peru coastal region for ICON (10 km / 5 km), ICON (160 km / 40 km), and ORAS5.** Columns show the three datasets, and rows show the annual mean and the DJF, MAM, JJA, and SON seasonal means over the available analysis period. Colors indicate mixed-layer depth, the solid black contour marks 50 m, and the dashed black line marks the offshore edge of the 0–200 km Peru coastal band. The spatial and seasonal variations provide context for interpreting the fixed 0–50 m process diagnostics as upper-ocean heat-content tendencies rather than mixed-layer tendencies.